AWARD NUMBER:

W81XWH-18-1-0412

TITLE:

Characterization of Acute Exposure to Toxic Metals in Military Environments and Personnel

PRINCIPAL INVESTIGATOR:

Todd Giorgio, Ph.D.

CONTRACTING ORGANIZATION:

Vanderbilt University, Nashville, TN

REPORT DATE:

October 2020

TYPE OF REPORT:

Annual Report

PREPARED FOR: U.S. Army Medical Research and Development Command
Fort Detrick, Maryland 21702-5012

REPORT DOCUMENTATION PAGE

Form Approved
OMB No. 0704-0188

1. REPORT DATE	**2. REPORT TYPE**	**3. DATES COVERED**
October 2020	Annual Report	01Sep2019-31Aug2020

4. TITLE AND SUBTITLE

Characterization of Acute Exposure to Toxic Metals in Military Environments and Personnel

5a. CONTRACT NUMBER

5b. GRANT NUMBER
W81XWH-18-1-0912

5c. PROGRAM ELEMENT NUMBER

6. AUTHOR(S)
Todd Giorgio, Ph.D.

E-Mail: todd.d.giorgio@vanderbilt.edu

5d. PROJECT NUMBER

5e. TASK NUMBER

5f. WORK UNIT NUMBER

7. PERFORMING ORGANIZATION NAME(S) AND ADDRESS(ES)

Vanderbilt University
2201 West End Avenue
Nashville, TN 37235

8. PERFORMING ORGANIZATION REPORT NUMBER

9. SPONSORING / MONITORING AGENCY NAME(S) AND ADDRESS(ES)

U.S. Army Medical Research and Development Command
Fort Detrick, Maryland 21702-5012

10. SPONSOR/MONITOR'S ACRONYM(S)

11. SPONSOR/MONITOR'S REPORT NUMBER(S)

12. DISTRIBUTION / AVAILABILITY STATEMENT

Approved for Public Release; Distribution Unlimited

13. SUPPLEMENTARY NOTES

14. ABSTRACT

Military personnel in modern conflicts are exposed to toxic metals from embedded fragments generated by explosive devices and inhaled near burn pits. Metal levels among veterans are centrally monitored, but to truly establish the impact of toxic metals on military personnel's health it is necessary to establish the peak exposure. No device exists to simultaneously detect and quantify multiple toxic metals in biological and environmental samples near the time of peak exposure. We hypothesize that a zinc oxide nanowire substrate decorated with gold nanoparticles and decorated with chelating ligands can sensitively detect toxic metals via surface-enhanced Raman spectroscopy (SERS). A patterned bed of ZnO nanowires will be grown and decorated with gold nanoparticles. Crown ethers identified based on selectivity for multiple toxic metals will functionalize the nanostructure. Sensitivity will be measured by parallel Raman studies of each selected ion coordinated with each crown ether, with and without plasmonic enhancement. Specificity will be assessed by SERS of each toxic metal in the presence of distractors. Selectivity of the crown ligands will be assessed by spectral analysis in the presence of distractors. Spectral analysis will also identify the optimal crown ethers for simultaneous, multiplexed sensing of the chosen toxic metals. Sensors in this optimized configuration will be fabricated and experimentally validated against predicted performance.

15. SUBJECT TERMS
None listed.

16. SECURITY CLASSIFICATION OF:			**17. LIMITATION OF ABSTRACT**	**18. NUMBER OF PAGES**	**19a. NAME OF RESPONSIBLE PERSON**
a. REPORT	**b. ABSTRACT**	**c. THIS PAGE**			USAMRMC
Unclassified	Unclassified	Unclassified	Unclassified	30	**19b. TELEPHONE NUMBER** *(include area code)*

TABLE OF CONTENTS

1. INTRODUCTION:

Military personnel in modern conflicts are exposed to toxic metals from embedded fragments generated by explosive devices and inhaled near burn pits. To truly establish the impact of toxic metals on military personnel's health it is necessary to establish the peak exposure, often during deployment in areas of conflict, in order to establish future health risk as well as identify those most needing of early therapeutic monitoring or interventional strategies to mitigate potential health risk. Contemporary methods to assess biologic and environmental metals exposure are limited, being either unsuitable for field analysis or limited to single-analyte detection. No device exists to simultaneously detect and quantify multiple toxic metals in biological and environmental samples near the time of peak exposure in the field. The goal of this project is to design a portable sensor based on a zinc oxide (ZnO) nanowire substrate decorated with gold (Au) nanoparticles and decorated with chelating ligands can sensitively detect toxic metals via surface-enhanced Raman spectroscopy (SERS). The first part of this study is the fabrication and functionalization of the sensing substrate. A patterned bed of ZnO nanowires will be grown and decorated with gold nanoparticles. Crown ethers will be amended to present sulfhydryl group(s) to enable strong association with the gold nanoparticles. Crown ethers will be selected for, and experimentally confirmed to possess selectivity for uranyl, cadmium, aluminum, and lead. These toxic metals represent among the most important in health outcomes from embedded fragments and serve as the proof-of-principle for future expansion of this approach. At each step in the fabrication process, the substrate will be characterized by multiple optical and spectroscopic techniques. Detection sensitivity will be measured by parallel Raman studies of each selected ion coordinated with each crown ether, with and without plasmonic enhancement. Detection specificity will be assessed by SERS of each toxic metal in the presence of other ions and distractors. Selectivity of the crown ligands will be assessed by spectral analysis in the presence of other metal ions and distractors. Spectral analysis will also identify the optimal crown ethers for simultaneous, multiplexed sensing of the four initial toxic metals. Sensors in this optimized configuration will be fabricated and experimentally validated against predicted performance.

2. KEYWORDS:

Crown Ethers; Zinc Oxide; Nanowires; Silver; Nanoparticles; Surface-Enhanced; Raman Spectroscopy; Microfluidics; Toxic Metals; Detection; Portable; Multiplexed; Trace; Polydimethylsiloxane; Chelation; Quantification

3. ACCOMPLISHMENTS:

What were the major goals of the project?

- **Major Task 1: Design and fabricate an advanced sensor for toxic metals based on zinc oxide nanowires decorated with nanoscale gold and functionalized with metal capture chemistry.**

- Subtask 1: Prepare a mask using electron beam lithography to spatially localize deposition of the seed layer necessary to support the growth of zinc oxide nanowires.

- Subtask 2: Prepare zinc nanowire forests by hydrothermal growth from previously discussed seed layer.

- Subtask 3: Decorate zinc oxide nanowires with nanoscale gold by electron beam deposition.

- Subtask 4: Assess zinc oxide nanowires with and without gold decoration using scanning electron microscopy (including atomic compositional information by EDX), photoluminescence, and UV-Vis spectrophotometry.

- Subtask 5: Functionalize gold nanoparticles using cyclic polyethers (crown ethers) of various sizes and geometries. Initial crown ethers will be dibenzo functionalized, which are commercially available from 15-crown-5 (15 atoms in the crown, five of which are oxygen) through 30- crown-10. Cyclic polyethers will amended to functionalize the cyclic polyether to the gold nanoparticles.

- Subtask 6: Assess cyclic polyether localization to the gold-decorated zinc oxide nanowires using scanning electron microscopy (including atomic compositional information by EDX) and infrared spectroscopy.

- **Major Task 2: Characterize sensor performance for the detection of toxic metals alone, in combination, and in the presence of known distractors present in biological and environmental samples.**

- Subtask 1: Measure the sensitivity of advanced sensors designed in Major Task 1 for detection of toxic metals with known military relevance. Selected toxic metal of interest will be measured over a range of relevant concentrations in the absence of other metals or potential sensing distractors in laboratory-scale Raman spectrometers, with appropriate parallel control studies.

- Subtask 2: Characterize the surface enhanced Raman signal amplification created by the interactions among cyclic polyether resonance and the gold nanoparticle surface, as enabled by careful quantitative calibrations and Raman spectroscopy measurements of cyclic polyethers and toxic metals in the absence of advanced sensors. Design a portable instrument based on solid state electronics for the multiplexed sensing of toxic metals at relevant concentrations.

- Subtask 3: Measure the specificity of advanced sensors for detection of toxic metals with known military relevance from explosive and burn pit exposures. Each toxic metal of interest will be measured over a range of relevant concentrations in the presence of other metals or distractors. These studies will be carried out in laboratory-scale Raman spectrometers with careful attention to quantitative characterization.

- Subtask 4: Computationally characterize the sensing of each toxic metal of interest in the presence and absence of other metals and sensing distractors. Select cyclic polyethers to provide optimal sensitivity and selectivity for each of the toxic metals of interest in a mixed sample over a relevant range of concentrations.

- Subtask 5: Prepare multiple advanced sensors on a single quartz substrate with each sensor functionalized with a different cyclic polyether as determined from Subtask 4.

- Subtask 6: Measure the specificity and selectivity of advanced sensors for detection of toxic metals with known military relevance from explosive and burn pit exposures. Each toxic metal of interest will be measured over a range of relevant concentrations in the presence of other metals or potential sensing distractors. These studies will be carried out in laboratory-scale Raman spectrometers with careful attention to quantitative characterization. Actual performance to be compared to performance predicted in Subtask 4.

What was accomplished under these goals?

Major Task 1, Subtask 1

Previously Reported: We designed and 3D-printed two masks shown in Figure 1. The mask shown in (a) was designed to spatially localize ZnO seed layer deposition to two spots in the central portion of the proposed microchannel. The mask shown in (b) was designed to spatially localize metal nanoparticle deposition to one of these spots. This was done in order to compare SERS with non-SERS measurements. Figure 2 demonstrates through UV-Vis absorption spectra acquired of seeded and non-seeded substrates after hydrothermal nanowire growth indicates that patterning the ZnO seed layer is sufficient to pattern subsequent ZnO nanowire growth. The band-edge shoulder at sub-400 nm wavelengths present in the spectrum acquired of the seeded substrate indicates crystalline ZnO consistent with the presence of nanowires while the lack thereof in the spectrum acquired of the non-seeded substrate indicates a lack of nanowire growth through the absence of crystalline ZnO. Over the course of experimentation, it was deemed more advantageous to mask the channel with Kapton tape such that only the channel was exposed to deposition. This subtask is complete.

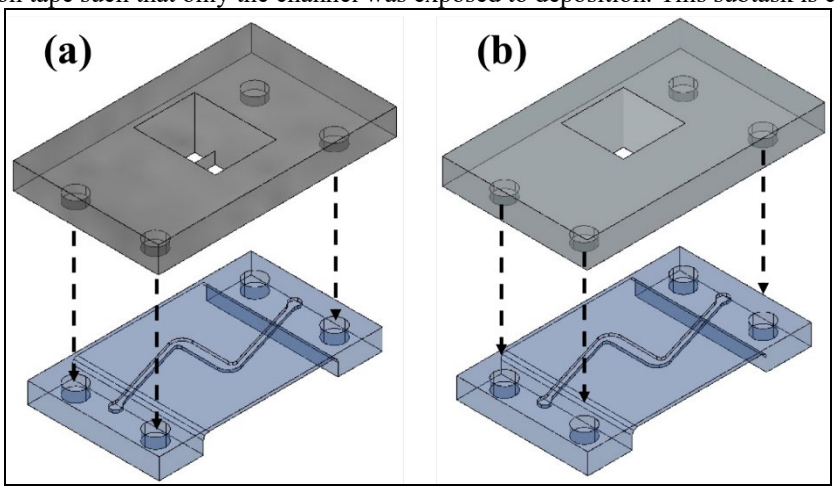

Figure 1: AutoCAD designs for masks to pattern deposition of (a) ZnO seed and (b) metal nanoparticles

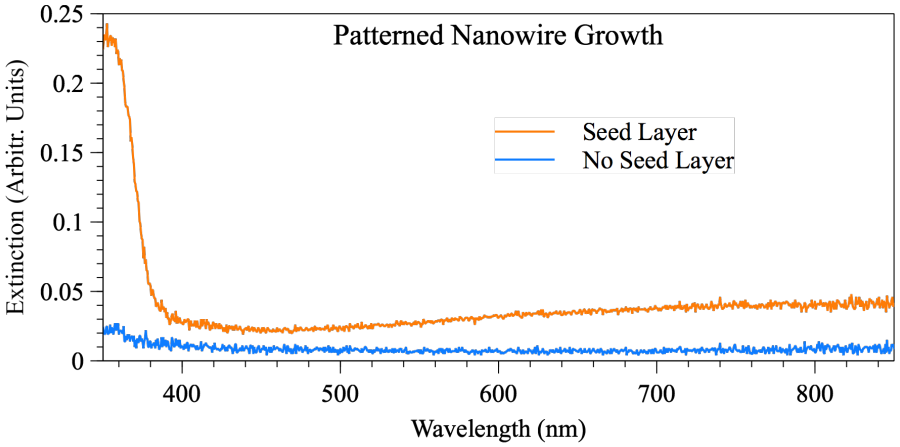

Figure 2: UV-Vis absorption spectra of ZnO-seeded and unseeded substrates following ZnO nanowire growth

Major Task 1, Subtask 2

Previously Reported: Nanowire forests have been grown successfully on PDMS substrates. 100-nm ZnO seed layers were deposited on both thick (~1 mm) and thin (<0.2 mm) PDMS substrates, from which highly crystalline ZnO nanowires were grown successfully, as shown by SEM and photoluminescence (PL) under Subtask 4. This indicates that nanowire growth inside a microchannel is possible.

New Results: Nanowires were successfully grown inside a PDMS channel, as shown by SEM and PL spectra under Subtask 4. A ZnO seed layer was deposited inside the channel via sputter deposition and annealed at 100 °C overnight. Nanowires were grown hydrothermally. This subtask is complete.

Major Task 1, Subtask 3

Previously Reported: After ZnO nanowires were successfully grown on PDMS substrates, silver nanoparticles were deposited onto the sides of the nanowires via electron beam deposition. Silver was chosen to form nanoparticles rather than gold because silver nanoparticles have a plasmon resonance in a 400-600 nm range of wavelengths, while gold nanoparticles' plasmon resonance tends to sit in the range of 600-800 nm. The Raman systems available for this research are better-suited for use with green lasers rather than red or NIR lasers. Gold can later be substituted for silver, should it prove necessary. The presence of Ag nanoparticles was demonstrated by both SEM images pre- and post-deposition, as well as by the presence of plasmon-based light absorption demonstrated by UV-Vis spectra acquired pre- and post-deposition. SEM and UV-Vis are both presented in Subtask 4.

New Results: A study was performed to optimize nanoparticle formation through deposition and anneal parameters to maximize surface enhancement within this paradigm. Through this study, it was determined that 7 nm of Ag deposited on ZnO at a rate of 0.1 Å/s and annealed at 50 °C for 2 hours resulted in the best surface enhancement, as demonstrated by Figure 3. Silver nanoparticles were successfully deposited on the sides of ZnO nanowires grown inside a PDMS microchannel. SEM and UV-Vis evidence of nanoparticle formation are presented in Subtask 4. This subtask is complete.

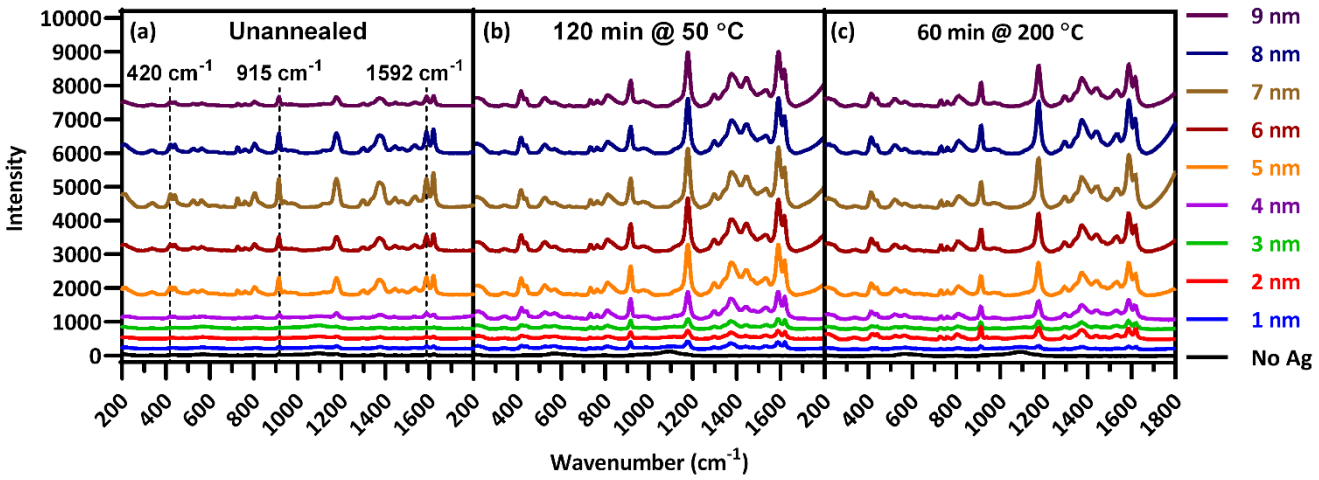

Figure 3: Raman spectra of crystal violet deposited on Ag-decorated ZnO substrates, of Ag thicknesses over a range of 1 – 9 nm and annealed at two different temperatures for two different times.

Major Task 1, Subtask 4

Previously Reported: As stated in Subtask 2, ZnO nanowires on PDMS substrates were assessed using PL (Figure 4) and SEM (Figure 5). The PL peak at ~385 nm in Figure 4 results from the wide direct-bandgap nature of crystalline ZnO and indicates the presence of highly crystalline ZnO nanowires. Furthermore, a lack of photoluminescent emission in the visible region indicates a lack of defects in the ZnO crystal structure. The SEM images of Figure 5 indicate that this highly crystalline ZnO indeed takes the form of nanowires. They also confirm the single crystal nature of the nanowires since they have a hexagonal cross-section consistent with the wurtzite crystal structure of ZnO.

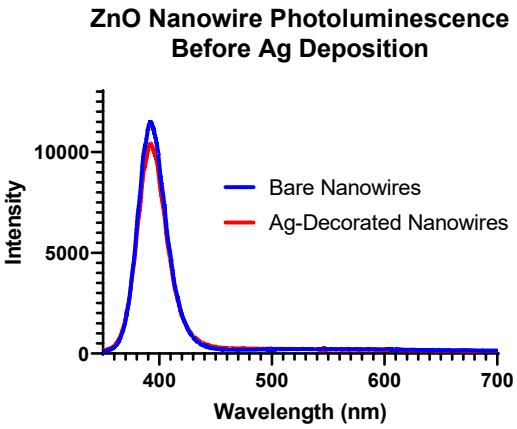

Figure 4: Photoluminescent spectra of ZnO nanowires, demonstrating high crystallinity and few defects

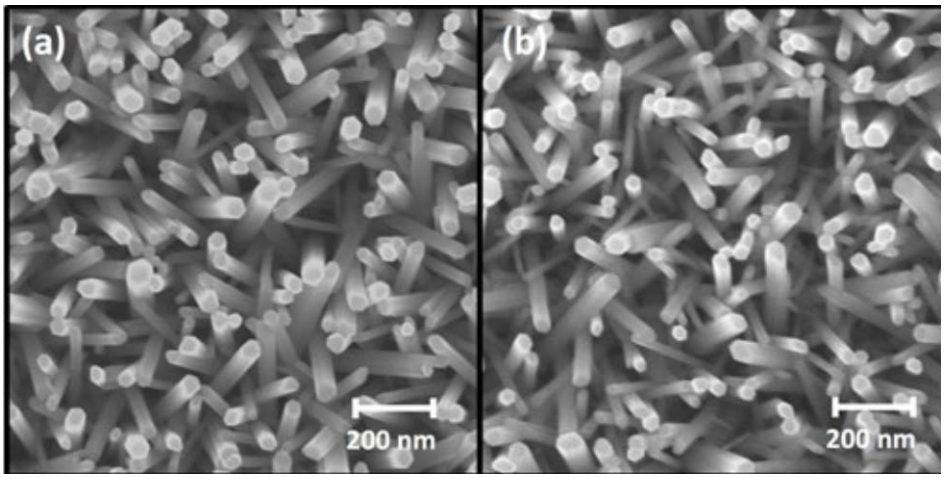

Figure 5: SEM images of ZnO nanowires, confirming single crystal nanowire formation

Previously Reported: As stated in Subtask 3, nanoparticle decoration on PDMS substrates was assessed using SEM imaging (Figure 6) and UV-Vis spectrophotometry (Figure 7). SEM images taken before and after nanoparticle deposition demonstrate the presence of nanoparticles on the sides of the nanowires. UV-Vis spectra acquired before and after nanoparticle deposition show the presence of a plasmon absorption peak centered at ~450 nm, consistent with Ag nanoparticle formation.

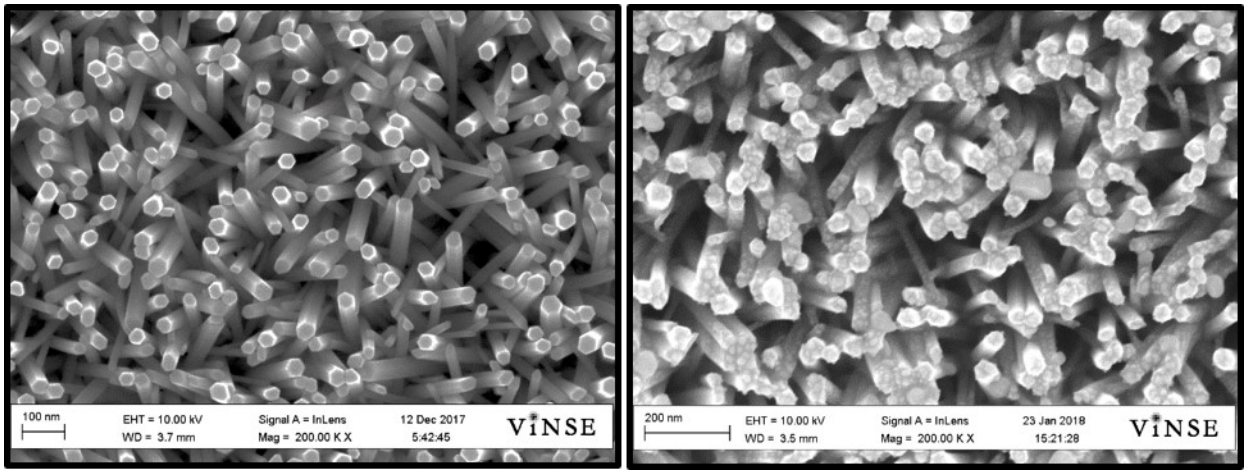

Figure 6: SEM Images of ZnO nanowires before and after nanoparticle deposition, showing the presence of Ag nanoparticles on the sides of the nanowires.

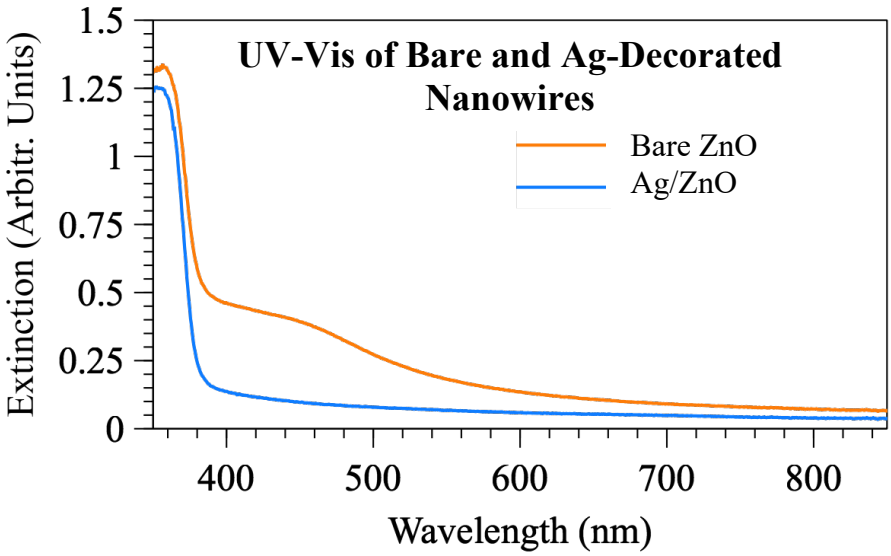

Figure 7: Extinction spectra of ZnO nanowires before and after Ag nanoparticle deposition

New Results: Nanoparticle decoration in the PDMS channel was assessed using SEM imaging (Figure 8) before and after Ag deposition and PL spectroscopy (Figure 9) before deposition. SEM confirmed nanowire growth and PL confirmed nanowire crystallinity. UV-Vis spectra acquired after nanoparticle deposition and anneal (Figure 10) show the presence of a plasmon absorption peak centered at ~515 nm, consistent with Ag nanoparticle formation. UV-Vis spectra acquired before and after nanoparticle anneal demonstrate change to the plasmon peak spread and wavelength. It was decided that atomic compositional information was unnecessary for this work as the presence of Ag had been demonstrated for this fabrication process in a previous work[1]. This subtask is complete.

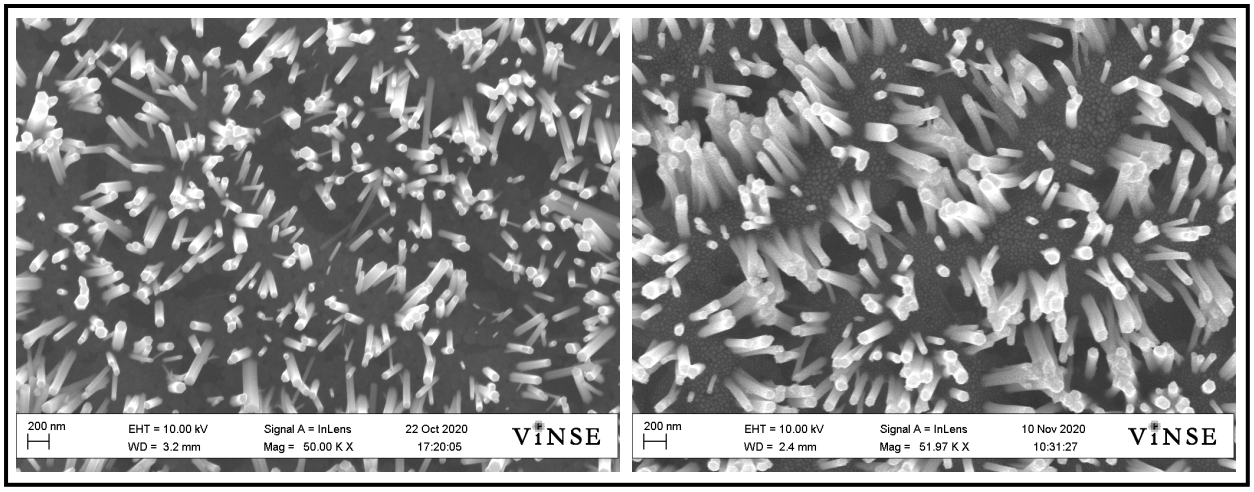

Figure 8: SEM images of ZnO nanowires inside PDMS microchannel before and after Ag nanoparticle deposition.

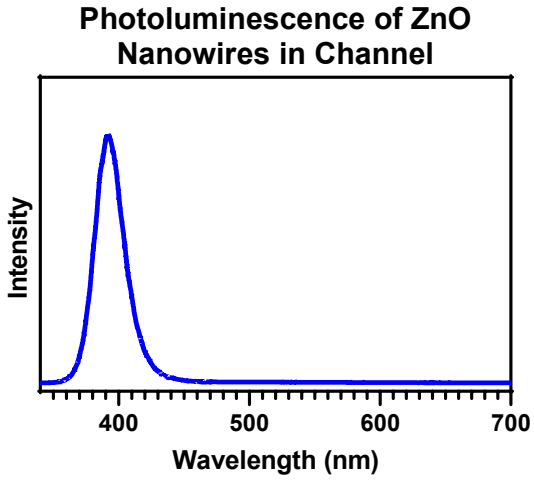

Figure 9: Photoluminescence spectrum of ZnO nanowires inside PDMS channel, demonstrating high crystallinity.

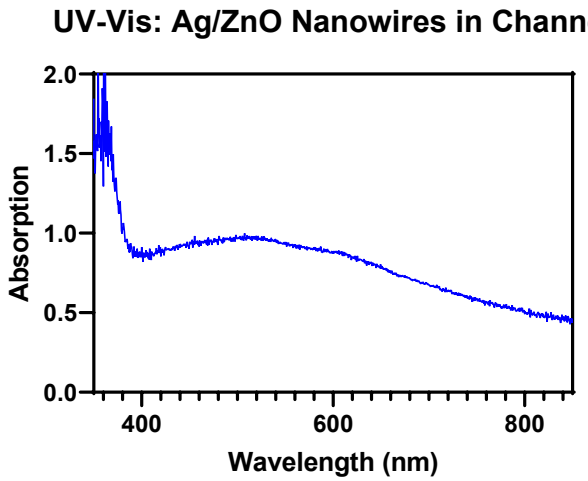

Figure 10: UV-Vis spectrum of Ag-decorated ZnO nanowires inside PDMS channel demonstrating plasmonic resonance.

Major Task 1, Subtask 5

New Results: Ag-decorated ZnO nanowires on a fused silica substrate were successfully functionalized with 4'-aminobenzo-18-crown-6 (AB18C6). The substrate was placed in a 104 µM solution of AB18C6 in 1:3 dimethyl sulfoxide (DMSO):DI Water. The solution was stirred for an hour, then left to incubate overnight. Samples of the solution before and after incubation with the substrate were acquired. Fluorescence and UV-Vis spectra were acquired of these samples and presented in Major Task 1, Subtask 6. Decoration of the SERS-active Ag/ZnO nanowires inside a channel is scheduled for Q1 of 2021

Major Task 1, Subtask 6

New Results: This subtask is dependent on success in Subtask 5. While SERS of crown ethers inside a PDMS channel has not been successfully demonstrated, SERS has successfully detected down 1 µM crystal violet in a PDMS channel (Figure 11). Functionalization of Ag/ZnO nanowires with AB18C6 was demonstrated by UV-Vis and fluorescence spectra in Figures 12 and 13 respectively as described in Major Task 1, Subtask 5. Both the absorption peak and fluorescence peak of AB18C6 in solution was reduced after incubation, indicating reduced concentration of AB18C6 in solution, demonstrating that AB18C6 decorated the Ag/ZnO substrate. Raman Spectra of Ag/ZnO substrates with and without AB18C6 were acquired in Figure 14, which demonstrated the presence of crown ether peaks. Demonstration of SERS of crown ethers in a PDMS channel is scheduled for Q4 of 2020.

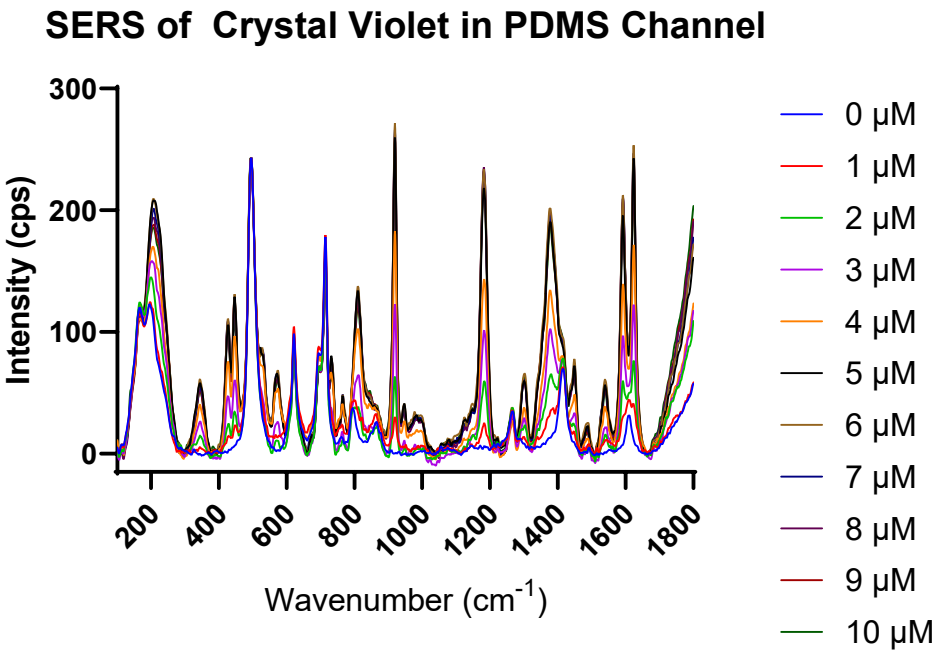

Figure 11: SERS of Crystal Violet over a concentration range of 1 – 10 µM, demonstrating the ability to do SERS through the PDMS wall of a channel.

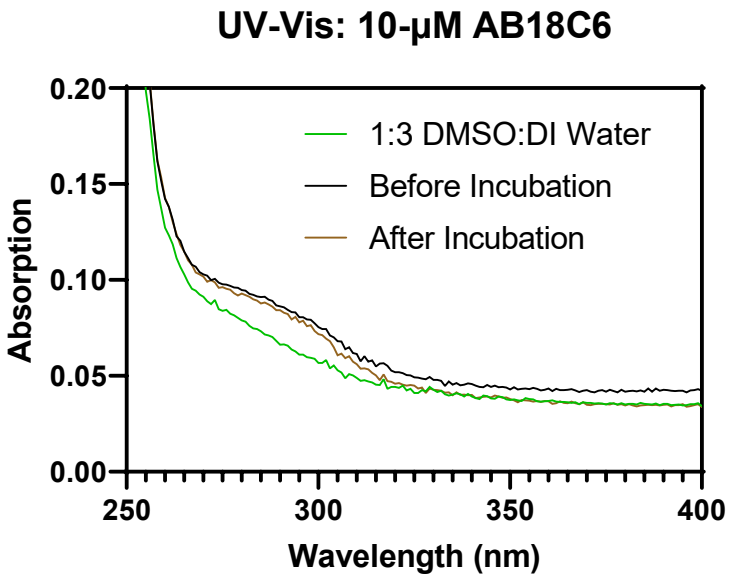

Figure 12: UV-Vis spectra taken of AB18C6 solution before and after incubation with an Ag/ZnO substrate, demonstrating decoration of the substrate with AB18C6 by reduced crown ether concentration in solution.

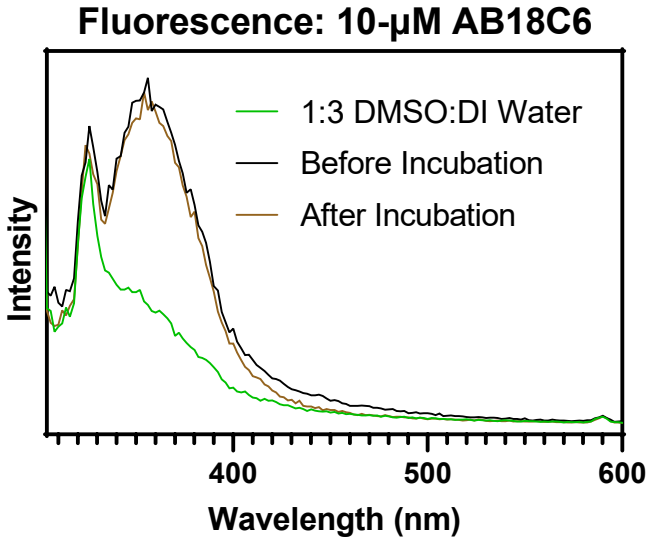

Figure 13: Fluorescence spectra taken of the AB18C6 solution before and after incubation with an Ag/ZnO substrate, demonstrating decoration of the substrate with AB18C6 by reduced crown ether concentration in solution.

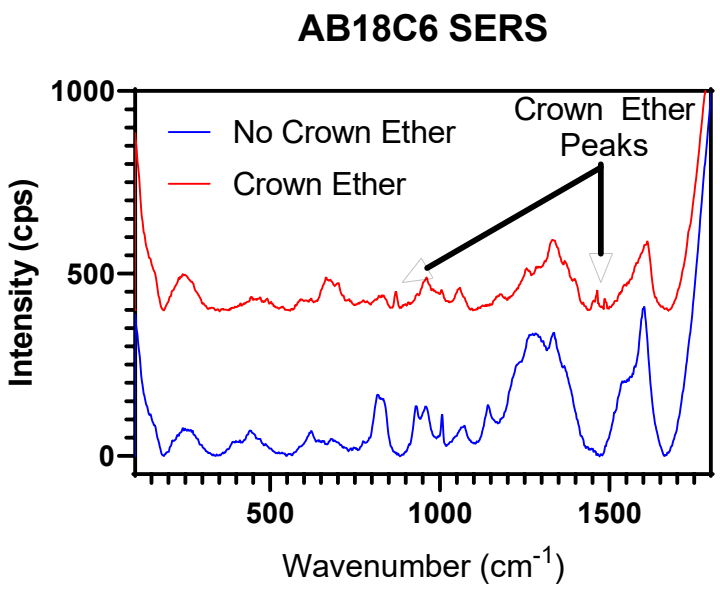

Figure 14: SERS spectra acquired of Ag/ZnO substrates with and without crown ether decoration, demonstrating clear presence of AB18C6 peaks.

Major Task 2, Subtask 1

Previously Reported: This subtask is dependent upon completion of Major Task 1. The nanowire-based sensor must be completed before true sensitivity of the sensor can be determined. However, work has been done toward using fluorescence as an additional sensitivity measure separate from SERS. Sarfo et. al. showed that 4'-aminobenzo-18-crown-6 has a broad fluorescence peak in the range of 300-400 nm when excited at 295 nm. When chelating metal ions, this fluorescence is quenched. We have had some difficulty replicating their results, but preliminary evidence shown in Figure 15 demonstrates that while the fluorescent peak of the crown ether is quenched in the presence of concentrations of arsenic and molybdenum ions equimolar to the crown ether concentration, it is not completely quenched. This indicates that fluorescence can be used as a check upon measuring SERS sensitivity. Completion of this subtask is scheduled for Q1 of 2021.

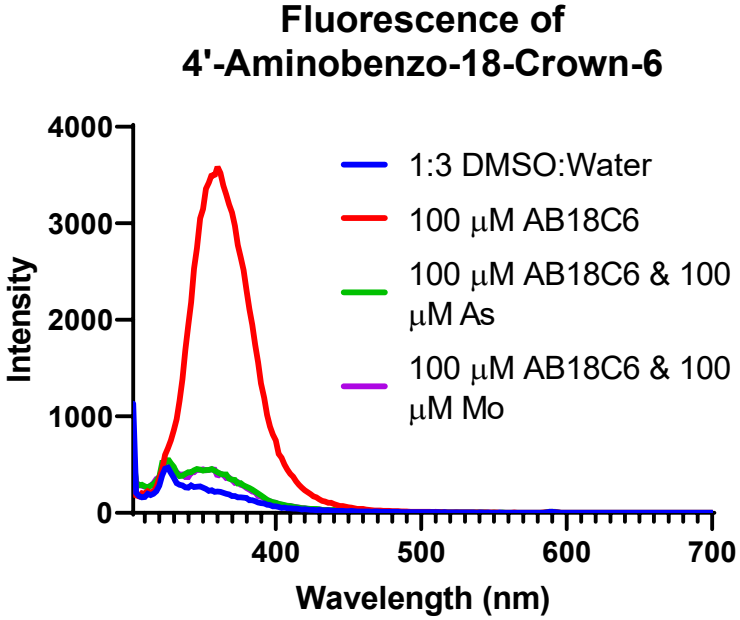

Figure 15: Fluorescence of 4'-aminobenzo-18-crown-6 with and without arsenic and molybdenum ions in a 1:3 DMSO:Water solution.

Major Task 2, Subtask 2

Previously Reported: This subtask is dependent upon completion of Major Task 1. However, it is important to determine whether acquiring Raman spectra through PDMS won't significantly interfere with the acquisition of crown ether spectra. To this end, Raman spectra were acquired of 25-µM crystal violet through Ag-decorated ZnO nanowires on PDMS. Two different thicknesses of PDMS were used. The "thick" PDMS was about ~1.0 mm while the "thin" PDMS was <0.2 mm. As shown in Figure 16, Raman spectra of crystal violet through the thick PDMS showed barely any enhancement, while spectra through the thin PDMS showed enhancement

comparable to our previous work, which acquired SERS spectra of crystal violet through fused silica. This indicates that as long as the thickness of the microchannel wall through which spectra are acquired is controlled, enhanced Raman spectra can be acquired. This subtask is scheduled to be completed in Q1 of 2021.

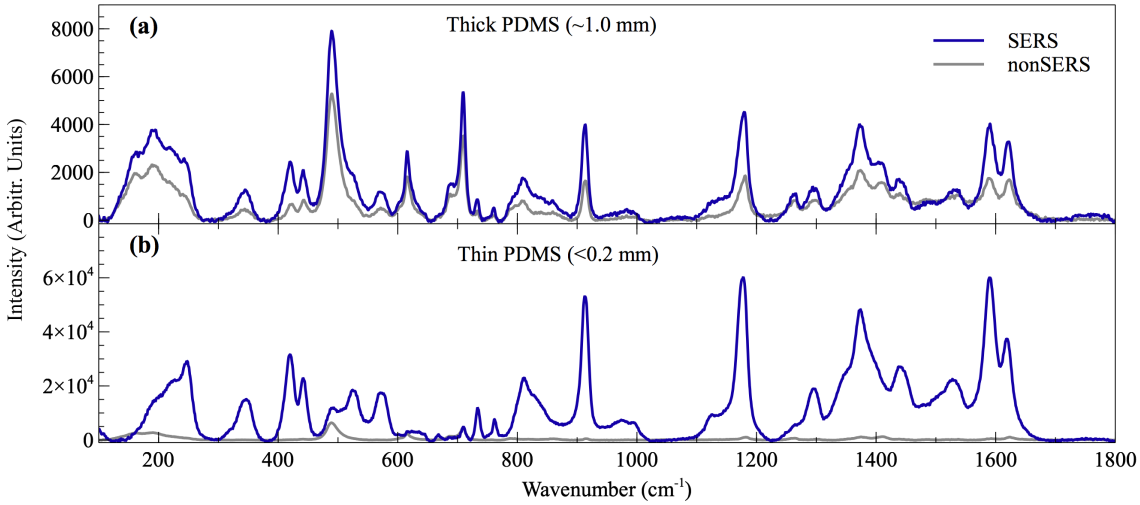

Figure 16: Raman spectra of 25 µM crystal violet through (a) thick PDMS and (b) thin PDMS

Major Task 2, Subtask 3

Previously Reported: This subtask is dependent upon completion of Major Task 1. However, the specificity of the crown ethers can be explored using UV-Vis spectrophotometry. Sarfo et. al. demonstrated that 4'-aminobenzo-18-crown-6 has an extinction peak around 300 nm. When the crown ether chelates a metal, this peak is reduced and a peak appears at about 280 nm. An optical extinction-based study was performed of the interactions between 4'-aminobenoz-18-crown-6 and a group of metal ions including metals on the Veteran's Association toxic metals biomonitoring panel, other toxic or potentially toxic metals, metals commonly found in the human body, and metals incorporated into the proposed biosensor. In total, this sweep included 22 metals and was performed in solutions of 1:1 DMSO:water and 1:3 DMSO:water (as performed by Sarfo et. al.). For the 1:1 DMSO:water solution (Figure 17), there was clear interactions between the crown ether and As, Hg, Al, Mo, Li, and W. For the 1:3 DMSO:water solution (Figure 18), Sarfo et. al. reported clear chelating of Pb, and none of Ba, Ca, Cd, Co, Cu, Hg, K, Li, Na, and Ni. However, we noted no discernable chelating of Pb. We did see chelating of several other metals including Mo, As, U, W, Cr, and Fe. This subtask is scheduled to be completed in Q1 of 2021.

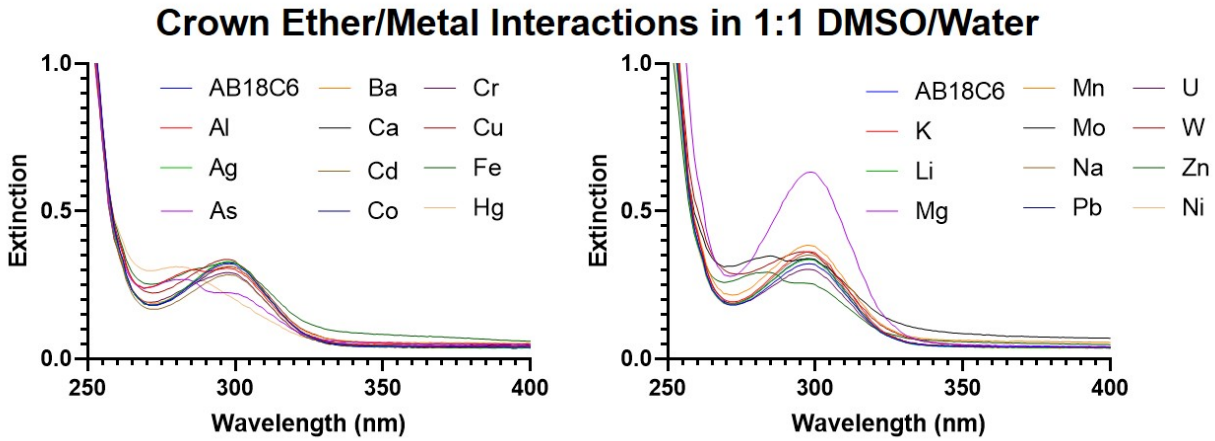

Figure 17: UV-Vis spectra of interactions between 4'-aminobenzo-18-crown-6 and 22 different metals in a 1:1 DMSO:water solution.

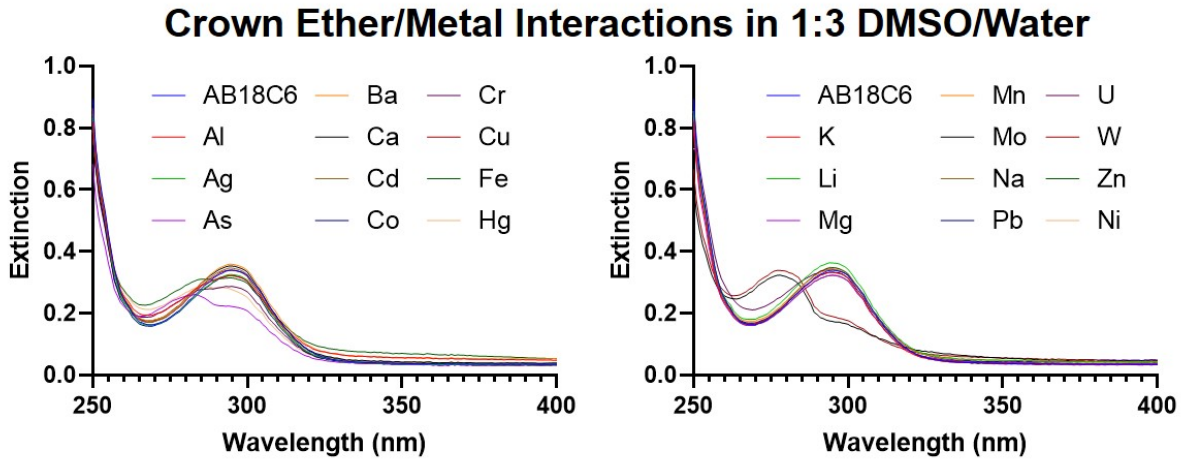

Figure 18: UV-Vis spectra of interactions between 4'-aminobenzo-18-crown-6 and 22 different metals in a 1:1 DMSO:water solution.

Major Task 2, Subtask 4
Completion of this subtask relies on the completion of Subtasks 2 and 3, to gather the information necessary for training an algorithm to identify chelated metals. This subtask is scheduled to be completed in Q1 of 2021.

Major Task 2, Subtask 5
Completion of this subtask requires completion of Subtasks 2 and 3 and is scheduled for Q1 of 2021.

Major Task 2, Subtask 6
Completion of this subtask requires completion of Subtask 4 and is scheduled for Q1 of 2021.

What opportunities for training and professional development has the project provided?

Nothing to report.

How were the results disseminated to communities of interest?

Describe how the results were disseminated to communities of interest. Include any outreach activities that were undertaken to reach members of communities who are not usually aware of these project activities, for the purpose of enhancing public understanding and increasing interest in learning and careers in science, technology, and the humanities.

Nothing to Report

What do you plan to do during the next reporting period to accomplish the goals?

A paper concerning the functionalization of the Ag-decorated ZnO nanowire substrate with 4'-aminobenzo-18-crown-6 and how the crown ether's Raman spectrum changes when it chelates different metals is being prepared. This paper is scheduled to be submitted in Q1 of 2021.

4. IMPACT:

What was the impact on the development of the principal discipline(s) of the project?
The paper reporting the optimization of electron beam-deposited Ag nanoparticles on ZnO for maximizing SERS represents a systematic examination of the fabrication and anneal parameters of such nanoparticles and will inform future fabrication of such nanoparticles for similar sensing paradigms.

What was the impact on other disciplines?

Nothing to Report.

What was the impact on technology transfer?

Nothing to Report.

What was the impact on society beyond science and technology?

Nothing to Report

5. CHANGES/PROBLEMS:

Changes in approach and reasons for change

New Changes: Kapton tape was used to mask the PDMS channel, rather than the previously described masks, as PDMS hydrophobicity unexpectedly hindered nanowire growth, requiring the entire channel to be coated in ZnO. For the same reason, ZnO seed was sputtered into the channel rather than deposited via e-beam. This was done in order to coat not only the bottom of the channel, but the walls in ZnO as well.

Previously Reported: Silver nanoparticles were deposited on the ZnO nanowires rather than gold, because silver nanoparticles have plasmon resonances in the 400-600 nm wavelength range, while gold nanoparticles have plasmon resonances in the 600-800 nm range. Additionally, silver tends to better enhance Raman spectra than gold. The facilities available for this research are better suited for lasers in the former range rather than the latter.

Actual or anticipated problems or delays and actions or plans to resolve them

Previously Reported: Difficulty has been encountered in replicating the results reported by Sarfo et. al. Specifically, while chelation of multiple metal ions (such as molybdenum and arsenic) by 4'-aminobenzo-18-crown-6 has been observed, this crown ether has failed to chelate lead ions, even under the same conditions reported by Sarfo et. al. Additionally, Sarfo reported in quantification of lead concentration via fluorescence[2]. Specifically, they reported a fluorescence peak at ~590 nm when excited at 295 nm that increased with increasing lead concentration. While the fluorescence of 4'-aminobenzo-18-crown-6 in Figure 7 exhibits a broad fluorescence peak between 300 and 400 nm that gets quenched when chelating molybdenum and arsenic, a sharp peak at 590 nm has not been observed. Based on the quenching in Figure 7, however, it is expected that this broad fluorescence peak can be used to quantify chelation via peak fluorescence quenching.

Previously Reported: In addition to our difficulties in replicating the results of Sarfo et. al., difficulty was encountered in ZnO nanowire growth. There came a point where nanowires stopped growing correctly. Instead of dense forests of nanowires as shown in Figures 4 & 5, nanowire growth was very sparse, as shown in Figure 11. After several weeks of troubleshooting, it was discovered that due to an aging quartz crystal microbalance in the electron beam deposition system being used, much less ZnO seed was being deposited than assumed. This resulted in replacement of the microbalance and nanowire growths performed since have reverted to a useful morphology.

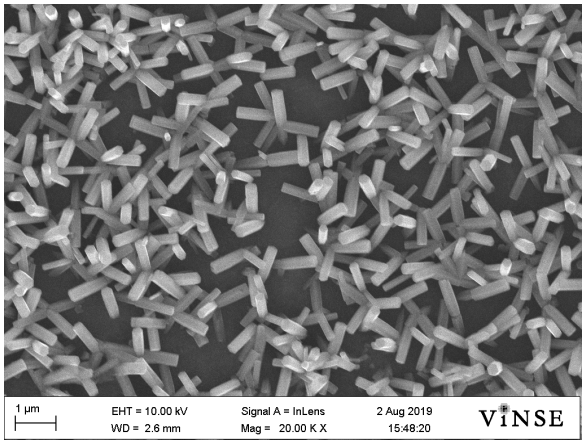

Figure 19: SEM image of sparse nanowire growth

Changes that had a significant impact on expenditures

Nothing to report.

Significant changes in use or care of human subjects, vertebrate animals, biohazards, and/or select agents

Significant changes in use or care of human subjects

Nothing to report.

Significant changes in use or care of vertebrate animals

Nothing to report.

Significant changes in use of biohazards and/or select agents

Nothing to report.

6. PRODUCTS:

- **Publications, conference papers, and presentations**

Journal publications.

Andrew L Cook, Christopher P Haycook, Andrea K Locke, Richard R Mu, Todd D Giorgio. Optimization of Electron Beam-Deposited Silver Nanoparticles on Zinc Oxide for Maximally Surface Enhanced Raman Spectroscopy. *RSC Nanoscale Advances.* Accepted 2020.

Books or other non-periodical, one-time publications.

Nothing to report.

Other publications, conference papers and presentations.

Nothing to report.

- **Website(s) or other Internet site(s)**

Nothing to report.

- **Technologies or techniques**

Nothing to report.

- **Inventions, patent applications, and/or licenses**

Nothing to report.

- **Other Products**

Nothing to report.

7. PARTICIPANTS & OTHER COLLABORATING ORGANIZATIONS

What individuals have worked on the project?

Name: Andrew Cook
Project Role: Graduate Student
Researcher Identifier (e.g. ORCID ID): ORCID ID: 0000-0002-2859-8804
Nearest person month worked: 12

Contribution to Project: Mr. Cook has performed all of the research reported here.
Funding Support: The National Science Foundation and this award.

Has there been a change in the active other support of the PD/PI(s) or senior/key personnel since the last reporting period?

Nothing to report.

What other organizations were involved as partners?

Fisk University provided facilities for this project.

8. SPECIAL REPORTING REQUIREMENTS

COLLABORATIVE AWARDS:

QUAD CHARTS:

9. APPENDICES:

Appendix A follows and contains the recently accepted manuscript generated from this project.

References

[1] A. L. Cook, C. S. Carson, C. E. Marvinney, T. D. Giorgio, and R. R. Mu, "Sensing trace levels of molecular species in solution via zinc oxide nanoprobe Raman spectroscopy: Zinc oxide nanoprobe Raman," *J. Raman Spectrosc.*, vol. 48, no. 8, pp. 1116–1121, Aug. 2017, doi: 10.1002/jrs.5180.

[2] D. K. Sarfo, E. L. Izake, A. P. O'Mullane, and G. A. Ayoko, "Molecular recognition and detection of Pb(II) ions in water by aminobenzo-18-crown-6 immobilised onto a nanostructured SERS substrate," *Sens. Actuators B Chem.*, vol. 255, pp. 1945–1952, Feb. 2018, doi: 10.1016/j.snb.2017.08.223.

Appendix A

Manuscript

Andrew L Cook, Christopher P Haycook, Andrea K Locke, Richard R Mu, Todd D Giorgio. Optimization of Electron Beam-Deposited Silver Nanoparticles on Zinc Oxide for Maximally Surface Enhanced Raman Spectroscopy. *RSC Nanoscale Advances.* Accepted 2020.

This manuscript remains in final production to correct a missing co-author, but is otherwise complete, including proof corrections. The attached preprint appeared on the *RSC Nanoscale Advances* website on 07 December 2020 as an *Accepted Manuscript*. D0NA00563K (rsc.org)

See next page.

ARTICLE

Optimization of Electron Beam-Deposited Silver Nanoparticles on Zinc Oxide for Maximally Surface Enhanced Raman Spectroscopy

Received 00th January 20xx,
Accepted 00th January 20xx

DOI: 10.1039/x0xx00000x

Andrew L Cook,[a] Christopher P Haycook,[a] Andrea K Locke,[a] Richard R Mu,[b] and Todd D Giorgio*[a]

Surface enhanced Raman spectroscopy enables robust, rapid analysis on highly dilute samples. To be useful, the technique needs sensing substrates that will enhance intrinsically weak Raman signals of trace analytes. In particular, three-dimensional substrates such as zinc oxide nanowires decorated with electron-beam deposited silver nanoparticles are easily fabricated and serve the dual need of structural stability and detection sensitivity. However, little has been done to optimize e-beam deposited silver nanoparticles for maximal surface enhancement in the unique dielectric environment of the zinc oxide substrate. Herein, fabrication and anneal parameters of electron beam-deposited silver nanoparticles were examined for the purpose of maximizing surface enhancement. Specifically, this work explored the effect of changing film thickness, deposition rate, anneal temperature, and anneal time on the surface plasmon resonance of Ag nanoparticles. In this study, multiple sets of fabrication and annealing parameters were discovered that optimized surface plasmon resonance for maximal enhancement to Raman signals acquired with a 532-nm laser. This work represents the first characterization of the fabrication and annealing parameters for electron beam-deposited silver nanoparticles on zinc oxide.

Introduction

There is an unmet multidisciplinary need for bioanalytical techniques that can perform analyses on small volumes of highly diluted specimens with minimum sample preparation. Applications such as the detection of toxic metals,[1–4] other pollutants or contaminants,[5–8] circulating tumor cells,[9] bacteria,[10] or viruses[11] benefit from fast and reliable molecular sensing. State-of-the-art tools used for these purposes such as high-performance liquid chromatography, mass spectrometry, and enzyme-linked immunosorbent assays commonly involve expensive reagents, large sample volumes, skilled technicians and frequently have low throughput rates. In addition, such tools are often plagued by limited differentiation among chemically or biologically similar analytes.[12–14] Raman spectroscopy is an attractive technique that addresses some of the limitations of other approaches because it provides a unique spectroscopic "fingerprint" of the biomolecular and biochemical composition of specimens, potentially offering effective detection and differentiation among analytes in minutes or seconds.[12–14] Raman also exhibits portability and facile function, as demonstrated by its use in forensic fields such as explosives identification.[18] However, Raman scattering has a small optical cross-section, with only one in 10^6 – 10^8 photons being Raman scattered, limiting its usefulness for trace analyte sensing. Surface-enhanced Raman spectroscopy (SERS), however, can significantly enhance intrinsically weak Raman signals, enabling reliable, efficient, and non-destructive detection of highly dilute analytes.

There are two mechanisms principally responsible for the enhancement effects in SERS. The first is electromagnetic and results from non-uniform local optical fields caused by surface plasmons of metal nanoparticles and nanostructured surfaces. In this mechanism, incident light drives the oscillation of electrons in the metal, which has a natural frequency dependent on the size, shape, dielectric environment, and material of the nanostructure. If this natural frequency matches the frequency of incident light, a resonant condition occurs, called a localized surface plasmon resonance (LSPR)[19] which can enhance the intrinsic Raman spectral intensity up to 12 orders of magnitude.[20] The second mechanism is chemically driven. Charge transfer takes place between metallic nanoparticles and adsorbed analytes, which can further enhance the intrinsic Raman signal as much as two orders of magnitude.[21] To take full advantage of surface enhancements, it is also necessary that the nanoparticles be spatially dense, to make use of "hotspots" in the gaps between nanoparticles.[22,23] For these reasons, much attention has been devoted to the use of metallic nanoparticles for incorporating SERS into various sensing system solutions. However, the expansive parameter space controlling SERS performance requires further investigation to effectively design sensors that provide optimal surface enhancement of intrinsically weak Raman signals.

Silver (Ag) is among the most commonly used metals for SERS-based sensing, due to strong Ag plasmon resonance in the visible region[24] and facile synthesis.[25] Many Ag nanostructures have been explored for SERS-based sensing, which fall into two basic categories: (1) colloidal nanostructures and (2) nanostructures on solid surfaces.[26] Colloidal nanostructures

[a] Department of Biomedical Engineering, Vanderbilt University, Nashville, TN 37235, USA
[b] TSU Interdisciplinary Graduate Engineering Research (TIGER) Institute, Tennessee State University, Nashville, TN 37209, USA

offer high sensitivity due to the ability to easily generate a large sensing surface area. However, due to random suspension of particles in free solution, colloidal nanostructures lack stability, and thus can affect measurement reproducibity. Conversely, nanostructures fabricated onto solid surfaces can possess great structural stability, resulting in greater measurement reliability. However, this stability comes at the cost of reduced sensitivity compared to colloidal paradigms due to lower surface area. This cost can be mitigated by fabricating inherently three-dimensional sensing substrates, as described in our previous work.[27] There are several methods of fabricating metallic nanoparticles onto a solid substrate that generally fall into two categories: chemical fabrication and physical deposition. Physical deposition techniques such as electron beam (e-beam) deposition facilitate formation of densely arranged Ag nanoparticles, enabling use of "hot-spots" between nanoparticles.[28] However, these techniques do not easily lend themselves to control of nanoparticle properties that affect LSPR. In the case of chemical fabrication, techniques such as hydrothermal growth are used to fabricate nanoparticles directly on the sensing surface.[29] While these techniques are more easily implemented and easier to control than physical deposition, they usually result in lower surface coverage by nanoparticles, reducing the impact of inter-particle hotspots. Therefore, by exploring the fabrication parameters that affect nanoparticle formation in physical deposition paradigms, greater control over nanoparticle formation can be implemented.

Recent research, including our own, has identified zinc oxide (ZnO) nanowires as a promising platform for SERS-active surfaces.[27,29–31] ZnO is a wide direct-bandgap semiconductor with a band-edge emission of 3.3 eV and a high exciton binding energy of 60 meV, making it electronically stable at room temperature.[32,33] These nanowires are also transparent to visible and near-infrared light,[34] which is ideal for Raman spectroscopy of biological samples. Additionally, ZnO possesses high electron mobility[35] and a large refractive index of approximately 2.0 in the visible region.[36] Combining these characteristics with the atomically smooth and highly faceted hexagonal single-crystal structure of the nanowires allows for wave-guiding of light, which can reduce signal loss due to light scattered away from the detector.[37] Nanowires also offer a greatly increased surface-to-volume ratio as compared to two-dimensional solid substrates. This increased surface area enables greater sensitivity in surface-based sensing techniques, such as SERS,[27,38] allowing solid substrates to approach the sensitivity of colloidal substrates while maintaining their inherent stability.

Previously, we prepared ZnO nanowires decorated with Ag nanoparticles for sensing soluble analytes. This sensing paradigm yielded an estimated six orders of magnitude surface enhancement of the Raman signal for crystal violet (CV, CCDC # 137090), melamine, and adenine.[27] Performance of this sensor was likely reduced because the Ag nanoparticles, with a plasmon peak at ~460 nm, were not optimal for SERS with the 532-nm laser used. We also did not explore the sensor performance as a function of Ag deposition parameters that are likely to influence SERS amplification mechanisms. Through this study, Ag-decorated ZnO nanowires demonstrated potential for effective sensing of trace analytes, which can be realized by examining the effect of fabrication and anneal parameters on surface plasmon resonance.

Parameters that can be manipulated during e-beam deposition of Ag and significantly impact the Raman enhancement include film thickness and deposition rate. Film thickness, in general, changes the shape and surface coverage of metallic nanostructures which changes LSPR characteristics of the film. By consequence, these changes modulate the magnitude of surface enhancement. Other research groups have explored how Ag nanoparticle plasmon resonance changes with film thickness in e-beam deposited[39] and sputtered[40] systems, but in neither of these works were nanoparticles deposited on a ZnO layer, which can significantly impact plasmon resonance as part of the dielectric environment of the nanoparticles. Also, while the effects of Ag film thickness on LSPR has been explored in some way, little attention has been devoted to the effects of Ag film deposition rate on plasmon resonance, even though deposition rate has a known effect on the structural properties of metallic films.[41] Furthermore, thermal annealing following deposition changes the nanoparticle size and shape through Ostwald ripening.[42] Since nanoparticle geometry and dimension are important drivers of plasmon resonance, thermal annealing offers an additional strategy for optimization of SERS sensing. Thermal annealing occurs as a result of two independent parameters: anneal temperature and anneal time.

In this work, four independently selectable parameters that influence Ag nanoparticle formation and presentation on ZnO were quantitatively controlled. These parameters, namely film thickness, deposition rate, anneal temperature, and anneal time were examined to assess their impact in modulating surface plasmon resonance. The functional consequences of these fabrication parameters were comparatively assessed using surface-enhanced Raman spectra that were acquired from crystal violet deposited onto each substrate. We aim to discover fundamental fabrication principles and sensor characteristics that will advance the design of maximally sensitive SERS devices based upon e-beam deposited Ag nanoparticles on a ZnO substrate.

Experimental

Substrate Preparation

Glass slides (Fisherbrand® Plain Microscope Slides) were cut into 80 1-cm^2 substrates with a diamond saw and cleaned by sonication sequentially for 10 minutes each in 1% aqueous Alconox® solution, deionized (DI) water, acetone, methanol, and again in DI water. Onto these substrates, a 100 nm ZnO layer was deposited via e-beam deposition at a rate of approximately 0.1 Å/s to ensure even deposition of Zn and O. As demonstrated by Figure S1, Masks were cut from aluminum foil large enough to completely cover the substrates, with a square cutout ~0.2 cm to a side, allowing a Ag film to be deposited on only a small portion of each substrate. After each

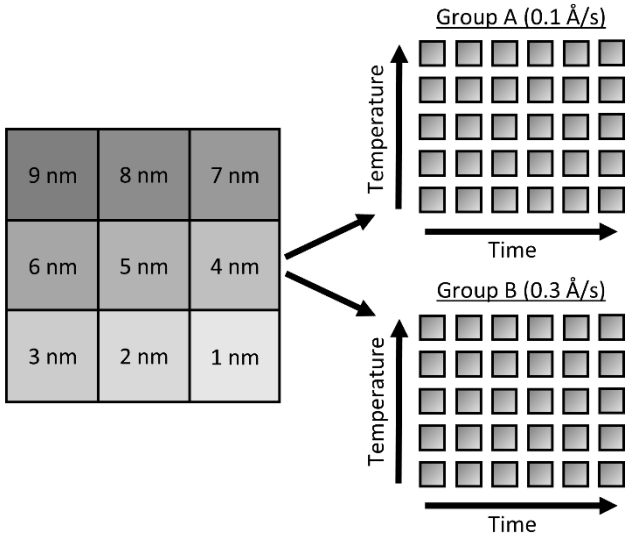

Figure 1: Schematic of substrates used for parameter exploration. Substrates deposited with 9 different Ag film thicknesses and separated into two rate groups (A and B). In each group, substrates are annealed over a range of times (15 – 150 min) and temperatures (50 – 400 °C)

film was deposited, the masks were shifted so that the cutouts exposed a new portion of each substrate, and a new film was deposited. This process was repeated nine times, for nine different Ag film thicknesses fit on each substrate, as illustrated by Figure S1. Ag thin films were deposited over a range of 1 nm to 9 nm film thicknesses, in 1 nm increments, hereafter referred to as T1 – T9. The 80 substrates were divided into two groups of 40 substrates, as shown in Figure 1. These two groups, hereafter referred to as Group A and Group B, were deposited with Ag thin films at rates of 0.1 and 0.3 Å/s, respectively. All Ag films in Group A were deposited at rates of 0.1± 0.002 Å/s and all Ag films in Group B were deposited at rates of 0.3 ± 0.018 Å/s. It is well known that when material from a point source is deposited onto substrates affixed to a flat plate, deposition rates fall off with axial distance from the source. This results in varying film thickness as a function of axial distance, defined by Equation (1):

$$t_d = \left[1 + \left(\frac{d}{R_0}\right)^2\right]^{-3/2} \quad (1)$$

In this equation, t_d represents the film thickness at distance d from the axis defined by the point source and R_0 represents the distance from the source to the plane of deposition. R_0 was measured to be 27 cm and the axial distance d of substrates farthest from the source was measured to be ~4.5 cm. Thus, the largest variation in film thickness was ~4% of the target thickness. All e-beam depositions were performed at pressures below 6.7 mPa.

Following the deposition of silver, the substrates were annealed at various temperatures: 50, 100, 200, 300 and 400 °C. At each temperature, different substrates were annealed at times: 15, 30, 60, 90, 120, and 150 minutes, providing a substrate from each deposition rate group (2 groups) with every anneal temperature (5) and time (6), producing 2 x 5 x 6 = 60 uniquely fabricated and annealed substrates and 1 unannealed control, each presenting T1 through T9 film thicknesses for a total of 549 different substrates.

Optical Characterization Techniques

Scanning electron microscopy (SEM) images, before annealing, were acquired of each Ag film thickness from a random substrate to get a visual perspective on the changing Ag nanostructure morphology as a result of changing film thickness. These images were acquired using a Zeiss Merlin scanning electron microscope (Jena, Germany) in a plan configuration with a 10 kV electron beam at a magnification of 200,000× and a working distance of 2.7 mm.

Extinction spectra were acquired of each film thickness, on each substrate before and after annealing, using a Hitachi U-4100 spectrophotometer integrating sphere to determine peak surface plasmon resonance wavelength. Extinction spectra were obtained at a rate of 3 nm/s over a range of 350 – 850 nm, with each substrate oriented facing away from oncoming light.

Raman spectra were acquired using a Thermo Scientific DXR Raman microscope (Waltham, MA, USA). A 532 nm diode-pumped, solid state (DPSS) laser was used with a 10x objective (Olympus, MPlan N Achromat, 0.25 NA) at a power of 10 mW as measured at the objective turret. Focal plane was adjusted before each acquisition to maximize spectral intensity. All substrates were placed in contact with a 25 µM aqueous solution of crystal violet (CV) overnight. The substrates were then removed from the CV solution and air-dried. Five Raman spectra were acquired from each substrate (T1-T9), along with five spectra of a portion on each substrate without Ag, hereafter referred to as T0. Each Raman spectrum was the accumulation of four background-subtracted spectra acquired over a range of 200-1800 cm^{-1}, each taken with a 5 s exposure time. All Raman spectra were acquired with a 50 µm pinhole aperture and a 900 grooves/mm grating.

Spectral Processing

UV-Vis spectra of the Ag films deposited on ZnO layers exhibit extinction from both Ag and ZnO. While ZnO is largely transparent in the visible region, light extinction due to the ZnO band edge occurs below approximately 380 nm. In order to accurately obtain Ag plasmon peak information, absorptive contributions from ZnO were approximated and subtracted as illustrated in Figure S2. To approximate ZnO absorptive contributions, UV-Vis spectra from the T1 portions of each substrate were fitted to a tri-gaussian equation, shown in Equation (2). In this fit, the first gaussian approximated the ZnO band-edge contribution, the second approximated the ZnO visible contribution, and the third approximated the Ag plasmon peak. T1 spectra were chosen for this task because of minimal overlap between the Ag plasmon peak and the ZnO band-edge and because the plasmon peak could be accurately approximated by a gaussian curve. Once fits to these spectra were successfully obtained, the third gaussian was subtracted from the fit to arrive at an approximation of the ZnO contribution to the spectra. This ZnO contribution for each substrate was then subtracted from the UV-Vis spectra for T1-

T9 for each substrate. Finally, a cubic smoothing spline, where Equation (3) is minimized, was fit to the resultant plasmon peaks to remove noise, enabling accurate extraction of plasmon peak extinction, wavelength, and spread.

$$F_g(x) = a_b e^{-\frac{(x-\mu_b)^2}{2\sigma_b^2}} + a_v e^{-\frac{(x-\mu_v)^2}{2\sigma_v^2}} + a_p e^{-\frac{(x-\mu_p)^2}{2\sigma_p^2}} \quad (2)$$

$$\lambda \sum_i [y_i - s(x_i)]^2 + (1-\lambda) \int_{x_{min}}^{x_{max}} \left(\frac{d^2 s(x)}{dx^2}\right)^2 dx \quad (3)$$

In Equation (2), F_g is the gaussian fit, a is an arbitrary fit parameter, and μ & σ represent the peak and root-mean-square width of the gaussian, respectively. Subscripts *b*, *v*, and *p* denote the gaussian fitting of the ZnO band-edge, ZnO visible, and Ag plasmon contributions to the spectrum, respectively. In Equation (3) λ represents the smoothing parameter, y is the set of observed extinctions at each wavelength, x is the set of wavelengths at which extinction is measured, s is the smoothed function output of the equation, and x_{min} & x_{max} are the minimum and maximum wavelengths of the spectrum, respectively. For this work, a smoothing parameter λ = 0.003 was used. A smoothing spline was used to approximate the plasmon rather than a gaussian because, while the plasmon peaks of thinner films could be accurately approximated by a gaussian fit, the plasmon peaks of thicker films could not due to increasing asymmetry in the peak. Spread was measured at the full width-half maximum (FWHM) of each plasmon peak where possible. For several spectra, particularly of thicker Ag, the FWHM was sufficiently broad to extend beyond the measured wavelength range and could not be determined. All processing of UV-Vis spectra was performed in MATLAB.[42]

Raman spectra were subtracted of their fluorescent background, estimated using 5th-degree polynomial fit. These spectra were then smoothed using a Savitzky-Golay filter. Each of the five spectra acquired from each film thickness (T0-T9) on each substrate were averaged to find a representative spectrum. Three CV Raman peaks at 420, 915, and 1592 cm^{-1}, tabulated in Table 1 with their associated vibrational modes and the CV molecular structure, were selected to provide specific, characteristic features for the estimation of enhancement factors (EFs). These peaks were selected to interrogate EFs from each end of the measured spectra and one feature near the middle of the spectra. The intensities of these peaks in the spectra for T1-T9 on each substrate were divided by the intensities of the same peaks in the spectrum of T0 on the same substrate to arrive at EFs for each peak.

Statistical Analysis

All error bars represent standard deviation unless otherwise stated. Two-way analysis of variance followed by Tukey's and Sidak's multiple comparison tests was performed for data presented here as indicated, and statistical significance was defined as $p < 0.05$. Statistical analyses were performed using Prism 7.04 (GraphPad Software).

Results & Discussion

The surface plasmon peak of a distribution of Ag nanoparticles possesses three characteristics that affect the level of enhancement: peak intensity, peak wavelength, and peak breadth. Because surface plasmons enhance both incident light from the laser and Raman-scattered light, surface enhancement is most effective when high plasmon extinction occurs at both the laser line and across the range of wavelengths at which light is scattered. Thus, the surface plasmon peak should be located near the laser line to maximize enhancement to incident light, and the peak should be sufficiently broad to provide significant enhancement to Raman-scattered light across the wavelength range of interest. In addition, plasmon intensity correlates with enhancement factor, with higher plasmon intensities generally producing greater enhancement for non-colloidal sensing substrates.[44] Surface plasmon peak intensity, wavelength, and breadth are all influenced by nanoparticle size, size distribution, crystal composition, proximity, and shape. These nanoparticle properties are modulated by deposition thickness and deposition rate, and by anneal temperature and time, post-deposition. In this study, we explore the combinatorial effect of these fabrication parameters on the surface plasmon peak characteristics of Ag nanoparticle arrays and correlate these effects to changes in enhancement of intrinsic Raman spectral intensity of CV. By doing so, we aim to facilitate the development of optimized sensing substrates for maximally surface-enhanced Raman spectroscopy.

Effect of Film Thickness on Surface Enhanced Raman Spectroscopy

Increasing Ag film thickness was anticipated to intensify, broaden, and red-shift the plasmon extinction peak due to increasing Ag surface coverage, increasing particle diameter, and decreasing interparticle distance. However, the quantitative relationships that describe these effects as a function of film thickness have not been previously described. Furthermore, while increasing intensity is correlated with

Table 1: The benzene and non-benzene vibrational modes of the CV peaks selected for analysis, with the CV molecular structure for reference

Raman Band (cm^{-1})	Non-Benzene Vibrational Modes	Benzene Modes
420	δ(C-C$_{center}$-C)/δ(C-N-C)$_{\parallel}$	16a
915	δ(C-C$_{center}$-C)	12,17a
1592		8a

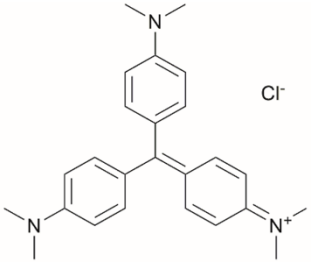

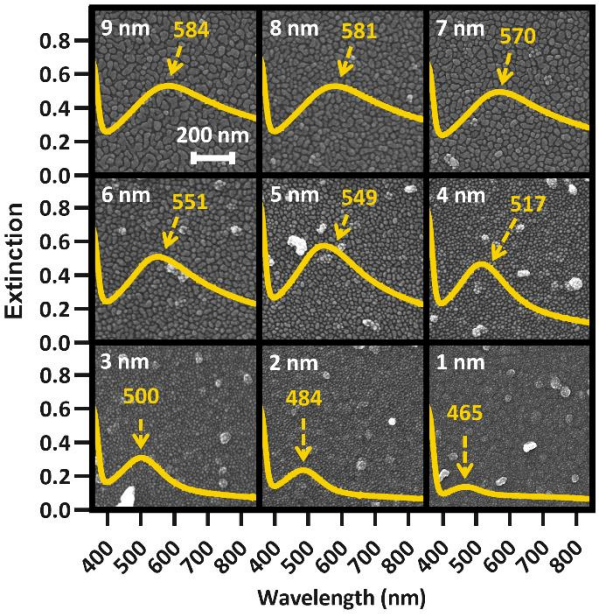

Figure 2: SEM images of all film thicknesses (identified in white) for a random substrate, with associated extinction spectra displaying peak plasmon wavelength overlaid. The plasmon peak wavelength is identified in yellow for each extinction spectrum.

increasing surface enhancement, for solid substrates, maximizing enhancement requires proximity of the peak wavelength with the incident laser. In addition, broadening the plasmon peak is only effective insofar as it maximizes plasmon extinction across the wavelengths of interest. Therefore, we examined the relationships between Ag film thickness and maximized surface enhancement through changes to nanostructure morphology and plasmon peak extinction characteristics. SEM images were acquired from Group A before annealing to explore the relationship between film thickness and nanostructure morphology. These images, shown in Figure 2**,** reveal that Ag was deposited as small islands that grow with increasing film thicknesses from 1 nm (T1) to approximately 5 nm (T5) and become more film-like for depositions of 6 nm (T6) and greater. This change is likely due to surface coverage approaching 100% as a result of increasing Ag mass per area. Extinction spectra are superimposed on each SEM image in Figure 2, confirming intensified and red-shifted extinction with increasing film thickness. The symmetrical plasmon peaks observed among the lowest Ag depositions (T1 – T4) are consistent with individual, spherical Ag nanoparticles. The transition toward nanostructured thin films (T5 – T9) was accompanied by increasingly exotic nanostructure shapes, associated with increasing asymmetry in the plasmon peaks.

The UV-Vis spectra for all 9 film thicknesses on each of 40 substrates in Group A were processed as described in the Experimental Section above to find peak extinction intensity, wavelength, and breadth in each case. Plasmon extinction intensity increased with Ag film thickness, as shown in Figure 3(a). Intensity increases approximately linearly for T1 – T5, but begins to approach an asymptotic maximum for T6 – T9. The reduction in differential extinction for high film thicknesses is confirmed by the lack of statistically significant differences between T7 & T8 and T8 & T9 as compared to T1 – T6 in which each thickness group was significantly different from every other thickness group. This change in behavior between thin and thick films correlates with proximity-induced hotspots. When adjacent nanoparticles are within a few nanometers of each other plasmonic coupling results in a hotspot between them, greatly increasing plasmon extinction.[22] For T1 – T5, plasmonic coupling between nanoparticles drove the growth in plasmon extinction intensity as interparticle distances decreased, exhibited by Figure 2. Beginning at T6 however, interparticle gaps ceased to decrease as Ag was deposited. At that point, plasmon extinction intensity began to plateau, which is consistent with Ag accumulation becoming the primary driver for increasing plasmon extinction.

Plasmon peak wavelength red-shifted with increasing Ag film thickness, shown in Figure 3(b), from well below the laser line at an average of ~464 nm for 1-nm films, to well past the laser line at an average of ~584 nm for 9-nm films. This redshift was likely due primarily to increasing nanostructure size, which correlated closely with increasing film thickness (Figure 2). Unlike intensity, maximizing surface enhancements requires proximity of the plasmon extinction peak and the laser wavelength, illustrated by the green line in Figure 3(b). The wavelength of peak plasmon extinction also influences surface enhancement, as the efficiency of optical coupling is enhanced when the laser line is near the plasmon peak. The closest alignment between peak extinction and the laser line was at 517 nm for T4 and 548 nm for T5. Additionally, variability in peak wavelength generally increased as films thickened, with standard deviation growing from 4.2 nm for 1-nm films to as much as 17.3 nm for 8-nm films. We speculate that this behavior is associated with the increasingly exotic nanostructure shapes associated with increasing film thickness.

Maximal surface enhancement requires LSPR with both incident laser light and wave-shifted scattered light. While enhancement is improved when the plasmon extinction peak is close to the laser wavelength, the peak should also be sufficiently broad to enhance wave-shifted scattered light across the fingerprint region which, for organic molecules, usually consists of some portion of the region between 200 and 2000 cm^{-1}. When a 532-nm laser is used to acquire Raman spectra, this fingerprint region translates to 537.7 – 595.3 nm, illustrated by the shaded region in Figure 3(b).[45–48] Thus, the sensing approach aims for a plasmon wavelength range that usefully overlaps with the entire spectral region of interest. To estimate breadth of the plasmon peak, the FWHM was determined where possible. FWHM of the plasmon peaks correlate with film thickness and range from ~104 nm for 1-nm films to more than 400 nm for 8-nm films, as shown in Figure 3(c). While this phenomenon provides a greater wavelength range with the potential for useful sensing at the largest deposition thicknesses, it complicated our ability to accurately characterize the FWHM. For substrates with T5 and T6 film thickness, a FWHM could be calculated for 39/40 spectrums. For T7, a FWHM could only be calculated for 14/40 spectra. For T8, a FWHM could only be calculated for 4/40 spectra, and for T9, no FWHM's could be calculated. This phenomenon correlated with the increasing

asymmetry of the plasmon peaks as films transitioned from individual nanoparticles to nanostructured films, shown in Figure 2. This increasing asymmetry was beneficial for maximizing surface enhancement due to greater plasmon resonance across the fingerprint region.

Analyses of individual plasmon characteristics indicated that the film thickness required to produce maximal surface enhancement would optimize the balance among plasmon extinction intensity, peak proximity to the laser line, and extinction intensity across the fingerprint region. Because these plasmon extinction characteristics interact in non-obvious ways to influence the overall Raman spectra enhancement, SERS spectra of CV adsorbed onto the Ag films were acquired and shown in Figure 4(a) to characterize the role of film thickness on surface enhancement. CV possesses multiple strong Raman peaks, tabulated in Table S1 with their associated vibrational modes, across a large portion of the fingerprint region,[56] Very little enhancement was observed for T1 – T4, with the T4 film resulting in less than 5-fold enhancement across the fingerprint region as compared to the T0 spectrum. This inconsequential enhancement likely resulted from a combination of low plasmon intensity (Figure 3(a)), inefficient coupling between the plasmon peak and the laser line (Figure 3(b)), and insufficient peak breadth to enhance wave-shifted light across the fingerprint region. However, enhancement notably increased starting at T5, with up to 15.8-fold enhancement as compared to the T0 spectrum at 1592 cm^{-1}. Maximal enhancement was found to occur for the T7 film, with up to 25.7-fold enhancement across the fingerprint region at 1592 cm^{-1}, before decreasing with T8 and T9 films. The diminished enhancement for the thickest Ag films is correlated with an increasing departure from the laser line due to red-shifting peak plasmon extinction (Figure 3(b)) accompanied by decreasing rate of plasmon extinction intensification (Figure 3(a)). These results are non-obvious when assessing plasmon peak characteristics individually, illustrating the value in analyzing relationships between these characteristics in light of how they influence surface enhancement. These results demonstrate that film thicknesses of 5 nm or greater provide the best surface enhancement, peaking with 7 nm film thickness. Thus, continued analysis focused on thicker films of 5 nm and above.

Effect of Annealing on Surface Enhanced Raman Spectroscopy

Following the analysis of deposition thickness, substrates were annealed to explore the effect of annealing temperature and time on plasmon extinction characteristics, toward additionally maximizing surface enhancement. From Group A, 31 substrates from Group A were chosen for this analysis, with the remaining 9 held in reserve should they be needed. Of the 31 substrates, one was set aside as an unannealed control and the remaining 30 were annealed at five temperatures in the range of 50 – 400 °C for six anneal times in the range of 15 – 150 min. Raman spectra were acquired of CV adsorbed onto Ag films after annealing, examples of which are presented in Figure 4(b,c). As

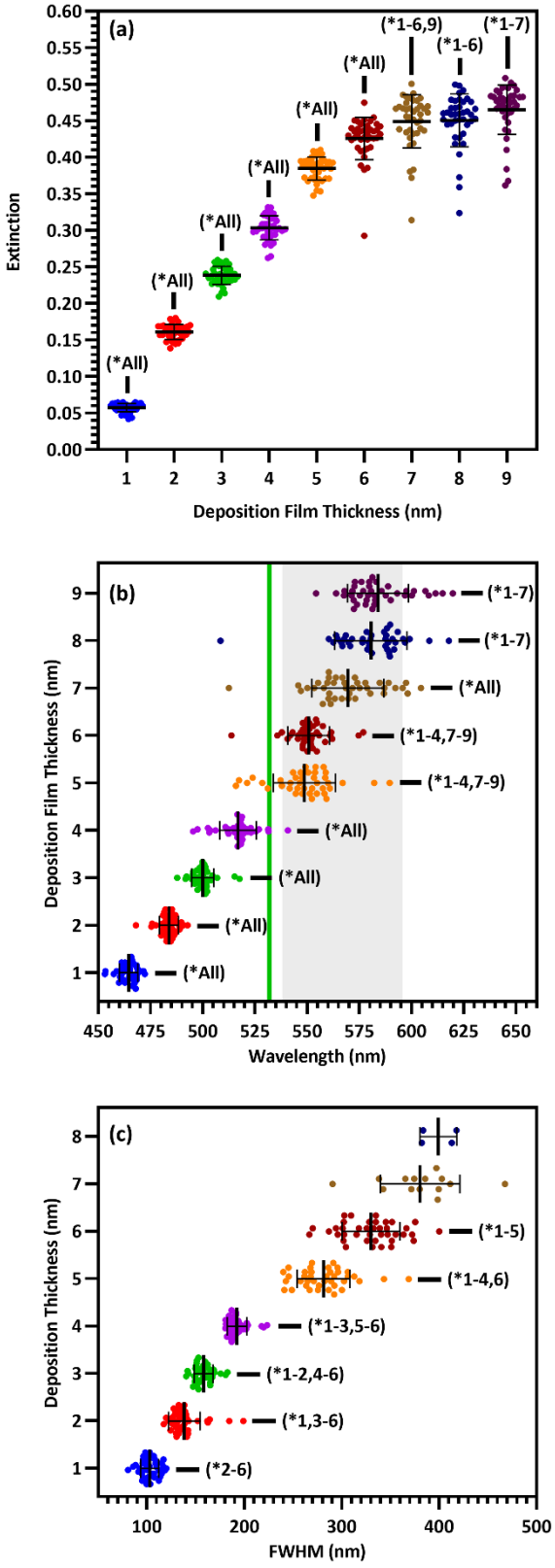

Figure 3: Scatterplots of plasmon peak (a) intensity (n = 40), (b) wavelength (n = 40), and (c) FWHM (T1 – T4: n = 40, T5 – T6: n = 39, T7: n = 14, T8: n = 4) for each film thickness of substrates in Group A. Green line and shaded region in (b) represent the laser line and fingerprint region, respectively. All data shown with mean and standard deviation of each group, *p <0.05 two-way ANOVA. Statistical significance of the FWHM of 7- and 8-nm films as compared to other films not shown due to an insufficient number of data points to use a parametric test.

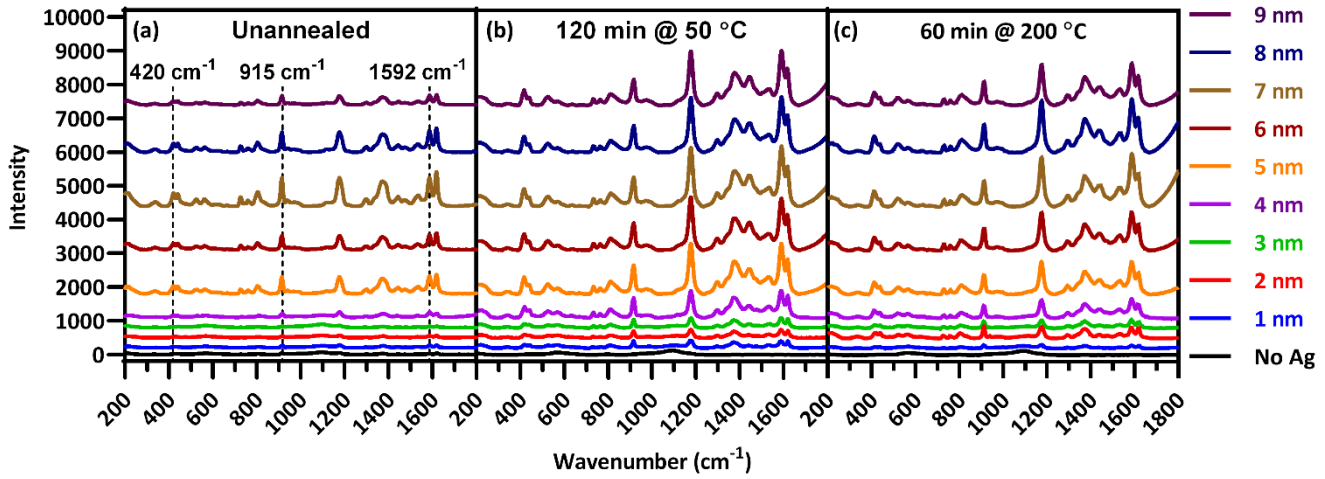

Figure 4: Raman spectra of CV deposited on each film thickness for substrates (a) unannealed, (b) annealed at 50 °C for 60 min, and (c) annealed at 200 °C for 60 min.

with the pre-anneal spectra in Figure 4(a), film thicknesses of 5 – 9 nm provided the best surface enhancement for both annealed substrates presented in Figure 4(b,c), peaking at 7 nm. However, the difference in surface enhancement between 7 nm and 5 or 9 nm films is much less pronounced for the annealed substrates than the unannealed substrate. Thus, annealing can be used to obtain near-maximum surface enhancement over a range of film thicknesses. Such flexibility in deposition thickness may be useful in cases such as three-dimensional sensing substrates like ZnO nanowires. In such cases, thicker films may over-fill interwire gaps, reducing effective surface area. Because maximal surface enhancement results in part from enhancement of Raman-scattered light across the fingerprint region, three CV peaks at 420, 915, and 1592 cm^{-1} as identified in Figure 4(a) were chosen to quantitatively assess enhancement at multiple points that span the fingerprint region. The enhancement of these peaks was calculated for T5 – T9 at each anneal temperature and time. These enhancements appear as a heat map in Figure 5, where red shading indicates increased enhancement. Annealing produced substantial impact to surface enhancement, but in ways that are nonlinear with respect to time and temperature. Annealing conditions generated changes to surface enhancements ranging from less than 3% to almost 3000% of the unannealed surface enhancement. Clearly, the selection of annealing parameters measurably impacts the performance of these sensors. Figure 5 reveals that annealing at 400 °C for even a short time drastically reduced surface enhancement across the board, indicating an

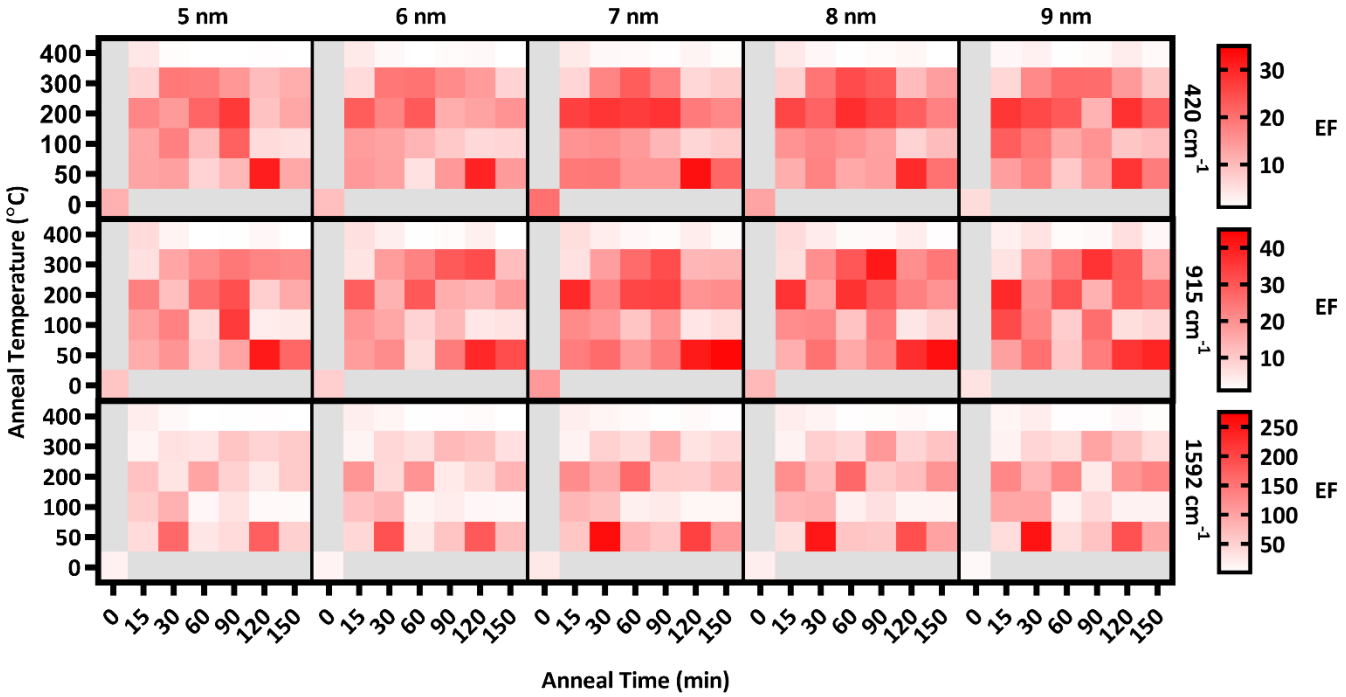

Figure 5: Heat map of the enhancement factors of T5 – T9 for 420, 915, & 1592 cm^{-1} peaks across all anneal temperatures & times along with the unannealed control.

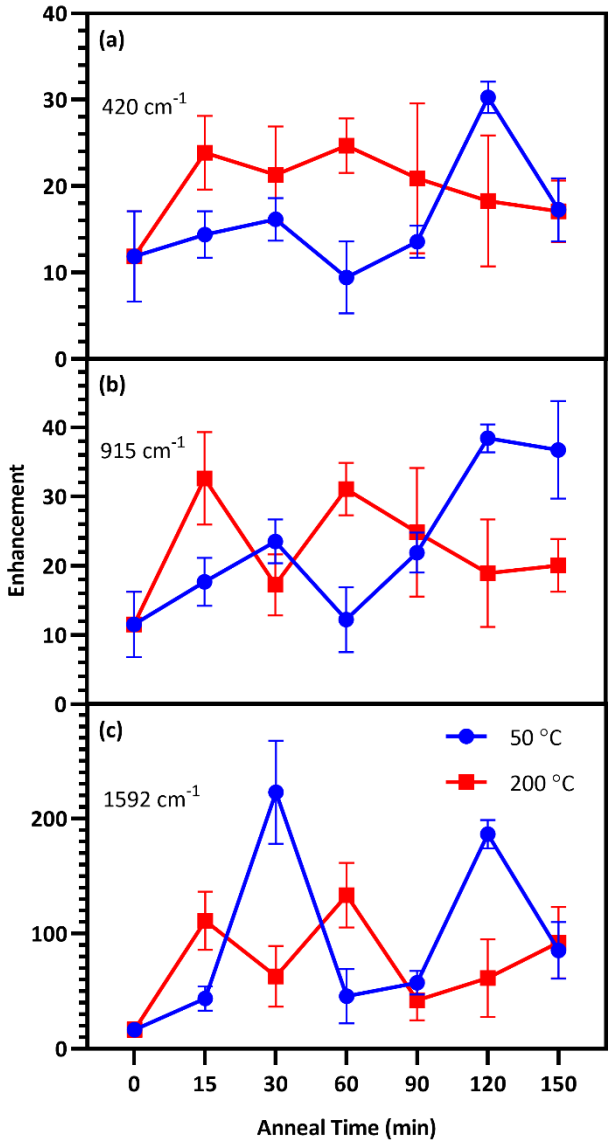

Figure 6: SERS EFs of substrates annealed at 50 °C (blue) and 200 °C (red) for up to 150 min, along with the unannealed control for the (a) 420 cm^{-1}, (b) 915 cm^{-1}, and (c) 1592 cm^{-1} peaks. Each point in the figure exhibits the mean and standard deviation of the EFs for T5 – T9.

upper temperature limit for this sensing paradigm well below 400 °C. Further examination of Figure 5 reveals that in general, the anneal time required to maximize surface enhancement decreased as anneal temperature increased. At 50 °C, maximizing enhancement required 120 min while at 100 °C, enhancement dropped off significantly after annealing 90 min. At 200 °C, enhancement was strongest when annealed from 15 – 60 min. Two of these anneal temperatures, 50 °C and 200 °C, produced particularly strong results toward maximizing surface enhancement, motivating closer examination.

Enhancement factors for the five film thicknesses were averaged for each anneal time at each temperature and plotted in Figure 6. The relative strength of enhancement between the two anneal temperatures varies across the three CV peaks, indicating the necessity of investigating enhancement across the entire fingerprint region. For instance, annealing at 30 °C resulted in opposing enhancement trends for the two anneal temperatures. Relative enhancement decreased farther away from the laser wavelength when annealed at 200 °C while it increased away from the laser wavelength when annealed at 50 °C. Among this variability, two anneal times produced consistently strong surface enhancement at these temperatures: 60 min at 200 °C and 120 min at 50 °C.

This study seeks to not only describe the deposition and annealing parameters that result in maximal surface enhancement, but also relate these results to changes in plasmon extinction characteristics effected by those fabrication parameters. To this end, changes to plasmon extinction characteristics for all five effective film thicknesses (T5 – T9) due to annealing at 50 and 200 °C were plotted in Figure 7. Annealing at 200 °C caused the plasmon intensity of all five film thicknesses to decrease steadily with increasing anneal time. In addition, annealing for 15 min or more at 200 °C blue-shifted the plasmon peaks. Annealing for 60 min slightly red-shifted the peaks, which blue-shifted again at higher anneal times (> 90 min). This blue-shifting behavior is consistent with increasing nanostructure uniformity due to Ostwald ripening, reducing the exotic nature of nanostructure shapes. FWHMs followed a similar behavior as peak wavelengths, with a short anneal time narrowing the plasmon peaks. These plasmon peaks widened slightly when annealed for 60 min before narrowing again beyond 90 min. These observations agree with the results in Figure 6, indicating that annealing at 200 °C generated the best combination of plasmon intensity, peak wavelength, and peak width at 60 min of anneal time.

Annealing at 50 °C for less than 60 min reduced peak intensity that rebounded for anneal times of 60 – 120 min. Peak wavelength blue-shifted slightly following annealing for less than 60 min at 50 °C before subsequent red-shifting for annealing times of 60 – 120 min. FWHMs for 5- and 6-nm films were increased with increasing anneal time. These results agree with the results in Figure 6 that indicate an optimum anneal time of 120 min at 50 °C.

Effect of Deposition Rate on Surface Enhanced Raman Spectroscopy

Deposition rate had a significant impact on plasmon peak wavelengths, with films deposited at 0.3 Å/s exhibiting significantly red-shifted peaks compared to a deposition rate of 0.1 Å/s for each film thickness examined, excepting 7 nm, as shown in Figure S3(b). We hypothesize that this behavior can be explained by rate-induced differences in the crystal structure of Ag nanoparticles, as deposition rate has been shown to effect such crystal properties as grain size, dislocation density, and twin boundary density in metallic nanostructures.[41] These results suggest that the plasmon characteristics of e-beam deposited Ag films are sensitive to deposition rates, as small changes can have a significant impact on important physical characteristics of the nanoparticles. These results also clearly indicate the trade-off between degraded sensor performance and the reduced deposition time achieved at elevated deposition rate.

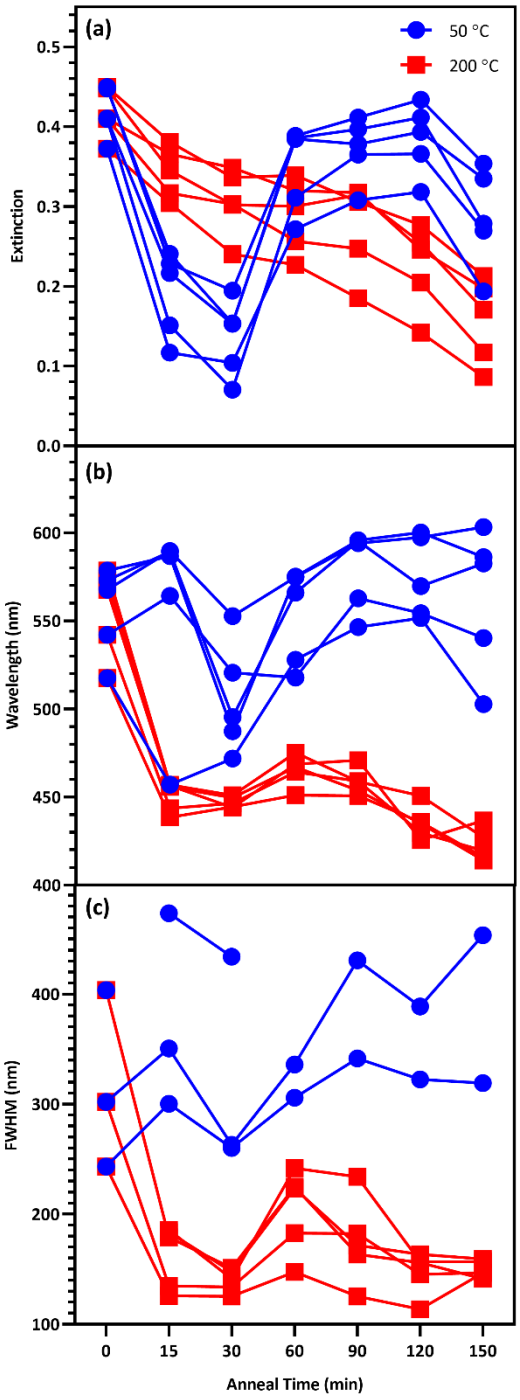

Figure 7: Change to the plasmon peak (a)intensity, (b)wavelength, and (c)FWHM due to anneal time at 50 °C (blue) and 200 °C (red) for T5 – T9.

While there was no significant difference in terms of enhancement in the unannealed controls between Groups A (0.1 Å/s) and B (0.3 Å/s), Figure S4 demonstrates that annealing the substrates in Group A generally produced more surface enhancement than Group B, across all film thicknesses, and anneal temperatures/times. This suggests that rate-induced differences in the crystal structure of Ag nanoparticles impacts annealing-induced effects on surface enhancement. This observation further emphasizes the important impact of deposition rate on the physical characteristics of Ag nanoparticles and the resulting surface enhancement of the structure.

Several combinations of fabrication and anneal parameters maximize surface enhancement by optimizing plasmon extinction. This study substantially improves the potential for fabricating high-performance sensors through elimination of fabrication parameters that yield low-enhancement materials. Importantly, these results demonstrate that maximal surface enhancement can be achieved by multiple different fabrication strategies. For instance, 2D sensing surfaces where film thickness does not impact device function have the best enhancement with a 7 nm thick surface deposited at 0.1 Å/s and annealed at 200 °C for 60 min. However, for 3D sensing surfaces such as the ZnO nanowire-based structure described in our previous work,[27] a thicker sensing surface could reduce device functionality by over-filling the spaces between nanowires, thereby reducing effective surface area. In such cases, a film approximately 5 nm thick, deposited at 0.1 Å/s and annealed at 200 °C for an hour is predicted to provide near-maximal surface enhancement without sacrificing sensing surface area. Another consideration is the substrate on which such nanostructures are fabricated. Many sensing strategies utilize substrates with high melting points such as glass or fused silica. In such cases, annealing at 200 °C is not problematic. However, increasing attention has been devoted in recent years toward fabricating SERS-active structures on flexible substrates made of materials like polyvinyl alcohol (PVA),[57,58] poly(dimethylsiloxane) (PDMS),[59] or polyvinylidene fluoride (PVDF).[60] In such cases substrates, even temperatures as low as 100 °C can have an undesirable effect on the substrate itself, such as increasing brittleness. For such device designs, excellent surface enhancement can be achieved by annealing substrates at 50 °C for 120 min.

Conclusions

This study provides guidance for the fabrication of sensors with maximal SERS enhancement excited with a 532-nm laser through e-beam deposited Ag nanoparticles on ZnO. 7-nm Ag films possess the optimal combination of plasmon peak intensity, wavelength, and breadth for maximal surface enhancement with a 532-nm laser. When 7-nm films are untenable, films as thin as 5 nm still provide near-maximal surface enhancement. We demonstrated that annealing at temperatures up to 200 °C for one to two hours further improved surface enhancement, but annealing at 200 °C for one hour or 50 °C for two hours resulted in the greatest increase to surface enhancement. Lastly, we discovered that Ag deposition rate significantly influences surface plasmon extinction peak characteristics. Increasing deposition rate from 0.1 to 0.3 Å/s resulted in decreased surface enhancement at all anneal times and temperatures, making 0.1 Å/s the clearly preferable deposition rate. The results presented in this study fill a vital need for guidance in determining fabrication and annealing parameters for maximal SERS with e-beam deposited Ag

nanoparticles with a 532-nm laser. We presume that similar fabrication relationships control the performance of other SERS substrates based on metal nanoparticles. This is the first report to begin to explore the impact of fabrication choices on the performance of a specific SERS sensor, but lays the groundwork for the assessment of similar phenomena in other Raman sensing approaches.

Conflicts of interest

There are no conflicts of interest to declare

Acknowledgements

A. L. Cook acknowledges support from the National Science Foundation Graduate Research Fellowship Program (NSF GRFP) 1445197. A. L. Cook and T. D. Giorgio also acknowledge support from the Congressionally Directed Medical Research Program (CDMRP) Peer Reviewed Medical Research Program (PRMRP) W81XWH-18-1-0412. C. P. Haycook acknowledges support from the National Heart Lung and Blood Institute (NHLBI) T32HL144446. R. R. Mu acknowledges support from the NSF Historically Black Colleges and Universities Research Infrastructure for Science and Engineering (HBCU-RISE) 1924241. The authors would like to thank Andrea Locke, Ph.D. for her input and support of this study. The authors would like to thank Eugene Collins, Ph.D. and Akira Ueda, Ph.D. at Fisk University for the use of their facilities and equipment. Lastly, the authors would like to thank Dmitry Koktysh, Ph.D. for his assistance and the Vanderbilt Institute of Nanoscale Science and Engineering (VINSE) for the use of their facilities and equipment in the course of this study.

Notes and references

1 D. K. Sarfo, A. Sivanesan, E. L. Izake and G. A. Ayoko, *RSC Adv.*, 2017, **7**, 21567–21575.
2 S. Jayabal, A. Pandikumar, H. N. Lim, R. Ramaraj, T. Sun and N. M. Huang, *Analyst*, 2015, **140**, 2540–2555.
3 M. S. Frost, Michael. J. Dempsey and D. E. Whitehead, *Sensors and Actuators B: Chemical*, 2015, **221**, 1003–1008.
4 Y. Zeng, J. Ren, A. Shen and J. Hu, *ACS Appl. Mater. Interfaces*, 2016, **8**, 27772–27778.
5 C. Rosman, J. Prasad, A. Neiser, A. Henkel, J. Edgar and C. Sönnichsen, *Nano Letters*, 2013, **13**, 3243–3247.
6 R. A. Halvorson and P. J. Vikesland, *Environmental Science & Technology*, 2010, **44**, 7749–7755.
7 W. F. Pearman, S. M. Angel, J. L. Ferry and S. Hall, *Applied spectroscopy*, 2008, **62**, 727–32.
8 N. E. Mircescu, M. Oltean, V. Chiş and N. Leopold, *Vibrational Spectroscopy*, 2012, **62**, 165–171.
9 X. Wang, X. Qian, J. J. Beitler, Z. G. Chen, F. R. Khuri, M. M. Lewis, H. J. C. Shin, S. Nie and D. M. Shin, *Cancer Research*, 2011, **71**, 1526–1532.
10 R. M. Jarvis and R. Goodacre, *Analytical chemistry*, 2004, **76**, 40–47.
11 A. A. Yanik, M. Huang, O. Kamohara, A. Artar, T. W. Geisbert, J. H. Connor and H. Altug, *Nano Letters*, 2010, **10**, 4962–4969.
12 A. Michelson, *Blood*, 1996, **87**, 4925–4936.
13 J. D. Driskell, K. M. Kwarta, R. J. Lipert, M. D. Porter, J. D. Neill and J. F. Ridpath, *Anal. Chem.*, 2005, **77**, 6147–6154.
14 H. Zhou, D. Yang, N. P. Ivleva, N. E. Mircescu, R. Niessner and C. Haisch, *Anal. Chem.*, 2014, **86**, 1525–1533.
15 I. Notingher, *Sensors*, 2007, **7**, 1343–1358.
16 A. Downes and A. Elfick, *Sensors (Basel, Switzerland)*, 2010, **10**, 1871–89.
17 N. Stone, C. Kendall, N. Shepherd, P. Crow and H. Barr, *Journal of Raman Spectroscopy*, 2002, **33**, 564–573.
18 D. S. Moore and R. J. Scharff, *Anal Bioanal Chem*, 2009, **393**, 1571–1578.
19 A. Campion and P. Kambhampati, *Chemical Society Reviews*, 1998, **27**, 241.
20 K. Kneipp, H. Kneipp, I. Itzkan, R. R. Dasari and M. S. Feld, *Journal of Physics: Condensed Matter*, 2002, **14**, R597–R624.
21 A. Campion and P. Kambhampati, 10.
22 J. D. Caldwell, O. J. Glembocki, F. J. Bezares, M. I. Kariniemi, J. T. Niinistö, T. T. Hatanpää, R. W. Rendell, M. Ukaegbu, M. K. Ritala, S. M. Prokes, C. M. Hosten, M. A. Leskelä and R. Kasica, *Opt. Express*, 2011, **19**, 26056.
23 K. Kneipp, H. Kneipp and J. Kneipp, *Acc. Chem. Res.*, 2006, **39**, 443–450.
24 D. Graham, K. Faulds and W. E. Smith, *Chem. Commun.*, 2006, 4363.
25 Y. Zhang, B. Walkenfort, J. H. Yoon, S. Schlücker and W. Xie, *Phys. Chem. Chem. Phys.*, 2015, **17**, 21120–21126.
26 P. Mosier-Boss, *Nanomaterials*, 2017, **7**, 142.
27 A. L. Cook, C. S. Carson, C. E. Marvinney, T. D. Giorgio and R. R. Mu, *J. Raman Spectrosc.*, 2017, **48**, 1116–1121.
28 B. H. Nguyen, V. H. Nguyen and H. N. Tran, *Adv. Nat. Sci: Nanosci. Nanotechnol.*, 2016, **7**, 033001.
29 Y. Xie, S. Yang, Z. Mao, P. Li, C. Zhao, Z. Cohick, P.-H. Huang and T. J. Huang, *ACS Nano*, 2014, **8**, 12175–12184.
30 S. Lee, S. H. Lee, B. Paulson, J.-C. Lee and J. K. Kim, *Spectrochimica Acta Part A: Molecular and Biomolecular Spectroscopy*, 2018, **204**, 203–208.
31 A. Tereshchenko, M. Bechelany, R. Viter, V. Khranovskyy, V. Smyntyna, N. Starodub and R. Yakimova, *Sensors and Actuators B: Chemical*, 2016, **229**, 664–677.
32 P. Yang, H. Yan, S. Mao, R. Russo, J. Johnson, R. Saykally, N. Morris, J. Pham, R. He and H.-J. Choi, *Advanced Functional Materials*, 2002, **12**, 323–331.
33 A. Janotti and C. G. Van de Walle, *Rep. Prog. Phys.*, 2009, **72**, 126501.
34 P.-H. Lei and C.-H. Cheng, *Materials Science in Semiconductor Processing*, 2017, **57**, 220–226.
35 Z. Kang, Y. Gu, X. Yan, Z. Bai, Y. Liu, S. Liu, X. Zhang, Z. Zhang, X. Zhang and Y. Zhang, *Biosensors & bioelectronics*, 2015, **64**, 499–504.
36 Y. S. Park and J. R. Schneider, *Journal of Applied Physics*, 1968, **39**, 3049.
37 D. C. Mayo, C. E. Marvinney, E. S. Bililign, J. R. McBride, R. R. Mu and R. F. Haglund, *Thin Solid Films*, 2014, **553**, 132–137.
38 Y. W. Heo, D. P. Norton, L. C. Tien, Y. Kwon, B. S. Kang, F. Ren, S. J. Pearton and J. R. LaRoche, *Materials Science and Engineering: R: Reports*, 2004, **47**, 1–47.
39 E. Thouti, N. Chander, V. Dutta and V. K. Komarala, *J. Opt.*, 2013, **15**, 035005.
40 S. Rezaee, *Results in Physics*, 2018, **9**, 1521–1524.
41 B. Amin-Ahmadi, H. Idrissi, M. Galceran, M. S. Colla, J. P. Raskin, T. Pardoen, S. Godet and D. Schryvers, *Thin Solid Films*, 2013, **539**, 145–150.
42 M. Bechelany, X. Maeder, J. Riesterer, J. Hankache, D. Lerose, S. Christiansen, J. Michler and L. Philippe, *Crystal Growth & Design*, 2010, **10**, 587–596.
43 *MATLAB R2019a*, The Mathworks, Inc., Natick, Massachusetts, United States.

44 Y. Nishijima, Y. Hashimoto, L. Rosa, J. B. Khurgin and S. Juodkazis, *Advanced Optical Materials*, 2014, **2**, 382–388.
45 J. Dunkers and H. Ishida, *Spectrochimica Acta Part A: Molecular and Biomolecular Spectroscopy*, 1995, **51**, 855–867.
46 A. Krylov, A. Vtyurin, P. Petkov, I. Senkovska, M. Maliuta, V. Bon, T. Heine, S. Kaskel and E. Slyusareva, *Physical Chemistry Chemical Physics*, 2017, **19**, 32099–32104.
47 C. A. Patil, I. J. Pence, C. A. Lieber and A. Mahadevan-Jansen, *Opt. Lett., OL*, 2014, **39**, 303–306.
48 H. Sato, H. Chiba, H. Tashiro and Y. Ozaki, *J. Biomed. Opt.*, 2001, **6**, 366.
49 J. Wang, X. Gao, H. Sun, B. Su and C. Gao, *Materials Letters*, 2016, **162**, 142–145.
50 M. V. Cañamares, C. Chenal, R. L. Birke and J. R. Lombardi, *J. Phys. Chem. C*, 2008, **112**, 20295–20300.
51 W. Meng, F. Hu, L.-Y. Zhang, X.-H. Jiang, L.-D. Lu and X. Wang, *Journal of Molecular Structure*, 2013, **1035**, 326–331.
52 T. Watanabe and B. Pettinger, *Chemical Physics Letters*, 1982, **89**, 501–507.
53 L. Angeloni, G. Smulevich and M. P. Marzocchi, *J. Raman Spectrosc.*, 1979, **8**, 305–310.
54 E. J. Liang, X. L. Ye and W. Kiefer, *J. Phys. Chem. A*, 1997, **101**, 7330–7335.
55 F. A. Harraz, A. A. Ismail, H. Bouzid, S. A. Al-Sayari, A. Al-Hajry and M. S. Al-Assiri, *Applied Surface Science*, 2015, **331**, 241–247.
56 S. Ju Cho, Y.-H. Ahn, K. Kumar Maiti, U. S. Dinish, C. Yaw Fu, P. Thoniyot, M. Olivo and Y.-T. Chang, *Chemical Communications*, 2010, **46**, 722–724.
57 D. He, B. Hu, Q.-F. Yao, K. Wang and S.-H. Yu, *ACS Nano*, 2009, **3**, 3993–4002.
58 C.-L. Zhang, K.-P. Lv, H.-P. Cong and S.-H. Yu, *Small*, 2012, **8**, 648–653.
59 A. J. Chung, Y. Suk Huh and D. Erickson, *Nanoscale*, 2011, **3**, 2903–2908.
60 T. K. Sinha, S. K. Ghosh, R. Maiti, S. Jana, B. Adhikari, D. Mandal and S. K. Ray, *ACS Appl. Mater. Interfaces*, 2016, **8**, 14986–14993.